MAX-PLANCK-GESELLSCHAFT

Freie Universität Berlin

Structural dynamics of transition metal dichalcogenide heterostructures studied by ultrafast high-energy electron diffraction

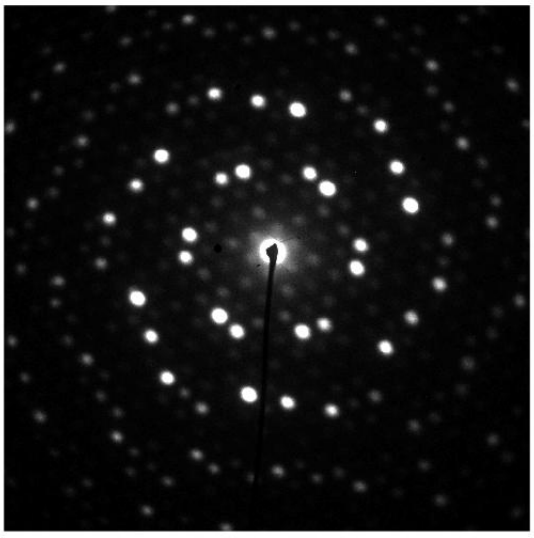

Master's thesis by

Daniela Zahn

Supervisors:
Dr. Ralph Ernstorfer (Fritz-Haber-Institut der Max-Planck-Gesellschaft)
Prof. Kirill Bolotin (Freie Universität Berlin)
Prof. Silke Christiansen (Helmholtz-Zentrum Berlin)

Abstract

We examine the structural dynamics of TMDC heterostructures with type-II band alignment after optical excitation using a pump-probe scheme. By driving the system under study out of equilibrium with a pump pulse and observing its response on ultrafast time scales, it is possible to learn about the coupling between the different subsystems of the structure (see Figure 1). In this work, we use electron diffraction to probe the lattice, a method which is sensitive to transient changes in the phonon population. Consequently, the energy transfer from the excited electrons to the lattice in the individual materials as well as the vibrational coupling between the two materials can be studied. Indirectly, the measurement is also sensitive to carrier transfer between the two materials. By observing the time-resolved structural response of the two lattices, we obtain information about the relaxation pathway of the system and the individual coupling strengths between the subsystems.

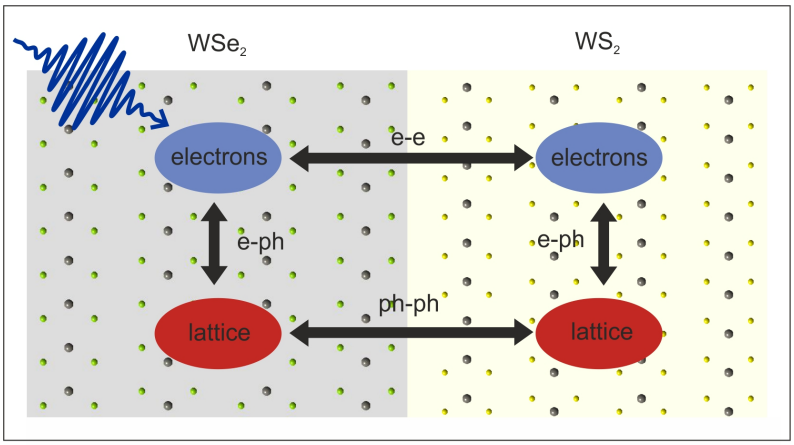

Figure 1: Sketch of a transition metal dichalcogenide (TMDC) heterostructure illustrating the coupling between the two different lattices and electronic systems.

Contents

1 Introduction

When graphene was discovered in 2004 by Konstantin Novoselov and André Geim [Nov04], it came as a surprise to most of the physics community. Until then, the common belief was that the existence of a stable layer with a thickness of only one atom was not possible. Soon, the potential of the new 'two-dimensional' material was realized and an entire new research field emerged. The properties of graphene are indeed intriguing: its unusual band structure with the linear dispersion relation at the K-point leads to a very high carrier mobility and an unusual Quantum-Hall-effect, for example. Furthermore, it is the strongest and at the same time most flexible material known to exist [Gei07]. Graphene has been suggested for numerous applications, for example for transistors, sensors, photovoltaic devices or even medical applications [Nov12]. However, for many applications, especially in electronics, the absence of a bandgap in graphene is disadvantageous. This, amongst other reasons, motivated the search for 'materials beyond graphene': shortly after the discovery of graphene, it was found out that other layered crystals can also be exfoliated to stable monolayers, among them transition metal dichalcogenides (TMDCs). In contrast to graphene, many TMDCs are semiconducting. While the bandgap of the bulk material is an indirect one, lowering the number of layers changes the bandstructure such that the monolayer exhibits a direct bandgap. This makes TMDC monolayers especially interesting for optoelectronic applications. In addition, the conduction band minima are strongly spin-split, with the spin polarization alternating between the six corners of the Brillouin zone (the K and K' points). Consequently, it is possible to excite only electrons with one spin by using circularly polarized light. This property is interesting for spintronic applications. Furthermore, the inequivalence of the K and K' points adds an additional degree of freedom, the so-called valley degree of freedom, which could in principle be used for information storage ('valleytronics'). On the other hand, TMDCs are also interesting from a fundamental point of view due to their very anisotropic, layered structure and because of the existence of strongly bound excitons in TMDC monolayers with binding energies of up to hundreds of meV [Che15].

Going one step further, different 2D-materials can be stacked to produce heterostructures. This is possible because the different layers are held together by van der Waals forces and can therefore be combined regardless of lattice constant mismatch. Moreover, the interfaces are atomically sharp. Figure 2 displays an scheme of such a vertical heterostructure. The combination of 2D materials with different properties opens up vast possibilities to design devices and even artificial materials, which can be customized to obtain the desired properties. The 'building blocks' for such devices range from insulating (hexagonal boron nitride) over semiconducting (many TMDCs) to conducting layers (graphene and some TMDCs). In addition, also the relative orientation between the layers can be used to tune the properties of the structure [Pur16].

Several devices made of TMDCs have already been realized in the lab, such as a diode, a transistor (see Figure 2(b)) [Roy15] and a solar cell [Flö15]. Apart from these 'conventional' applications, due to the unique properties of TMDCs, it is also possible to realize devices and that are not achievable using other materials. Figure 2 (c) sketches an efficient photovoltaic device exploiting the different band gap sizes of TMDCs. A similar stacking could be used to build a very small spectrometer.

In general, all these devices are operated in non-equilibrium conditions. Their behavior is therefore governed by the interaction between between the different subsystems of the crystal: electron-electron interaction, electron-phonon interaction, phonon-phonon

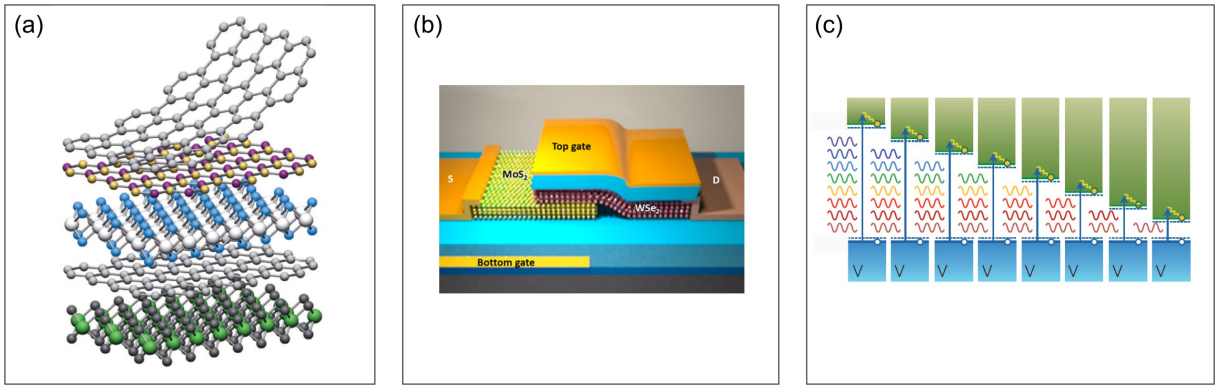

Figure 2: Panel (a) shows a scheme of a heterostructure made from different two-dimensional crystals. From [Gei13]. Panel (b) sketches a dual gated MoS2/WSe2 transistor recently realized in the lab. From [Roy15]. Panel (c) shows a proposed photovoltaic device. The design minimizes thermalization losses by stacking semiconducting layers with decreasing band gaps. From [Pol12].

interaction and the interaction between spins. In order to design devices or materials with the desired properties, it is of fundamental importance to know the efficiencies of the different interactions. To study this, we drive the system out of equilibrium by transferring energy to one of its subsystems (pumping). By observing the relaxation of the system back to equilibrium, information on the interactions is obtained.

Since the relaxation processes in a solid happen on the femto- to picosecond time scale, pump-probe experiments are the only way to access the dynamics of the system. We use a femtosecond electron diffraction setup to investigate the structural dynamics of the heterostructures after electronic excitation. As electron diffraction probes the long-range order of the sample, this method is sensitive to distortions of the lattice caused by phonons. Consequently, it is possible to observe changes in phonon population after excitation. This contributes to understanding the relaxation pathway of the excited carriers and allows to draw conclusions about the carrier-phonon coupling in the sample. The method has already been applied successfully to thin layered crystals such as graphene [Cha14] and WSe_2 [Wal16b]. In comparison, the study of heterostructures with electron diffraction is a conceptually new approach. For single-crystalline materials, it is possible to observe the dynamics of the two materials separately. Hence, energy transfer processes across the interface can be studied. Our experiments also serve as a proof of concept for this new approach.

We focus on TMDC heterostructures with staggered (type-II) band alignment. In this case, after excitation, charge is transferred between the layers, leading to charge separation across the interface [Zhu15]. This is interesting both for applied and fundamental research. Many applications, such as photovoltaic devices, require a type-II band alignment.

In the following, at first an introduction to the structural and electronic properties of TMDCs is given, followed by an introduction to vertical heterostructures made of layered crystals. Subsequently, the theory necessary to understand the diffraction patterns of heterostructures is presented. Finally, the results of time-resolved measurements on WS_2/WSe_2 heterostructures are presented and discussed.

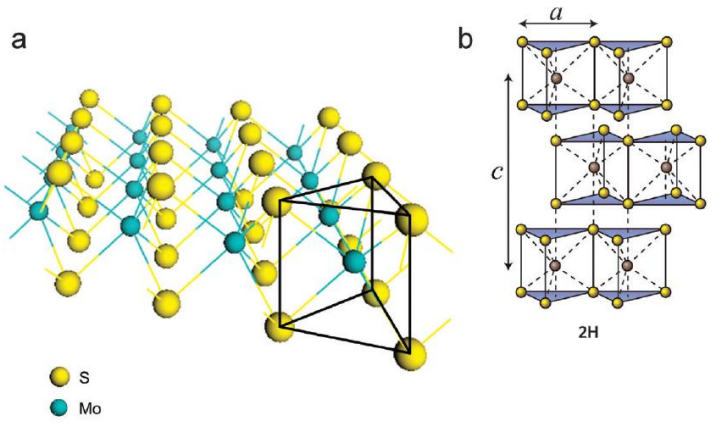

Figure 3: Panel (a) shows the structure of the TMDC crystals examined in this work (WSe_2 and WS_2). Two planes of chalcogen atoms enclose one plane of transition metal atoms. The coordination is trigonal prismatic. The stacking of the crystal used in this work is 2H, as shown in Panel (b). From [Zha15].

2 Transition metal dichalcogenides (TMDCs)

2.1 Lattice structure

Transition metal dichalcogenides have the chemical composition formula MX_2, with M being a transition metal (often Mo or W, but also for example Zr, V, Ta or Hf) and X being a chalcogen, that is S, Se or Te. A plane of transition metal atoms together with two planes of chalcogens form one layer. Within one layer, the atoms are bonded covalently, while the layers are held together by van-der-Waals interaction.

There are two possible types of coordination of the chalcogen atoms, trigonal prismatic and octahedral. The coordination strongly influences the electronic properties and also changes the stacking order of the layers [Zha15]. The crystal structure of the TMDCs examined in this work has a trigonal prismatic coordination and 2H stacking. This is shown in Figure 3.

2.2 Electronic band structure

As an example for the electronic band structure of the TMDCs examined in this work, Figure 4 shows the band structure of WSe_2. The band structure of WS_2 is qualitatively very similar, only the magnitude of the band gap is different. An important point in the band structure is the Σ point, the conduction band minimum of the bulk crystal. Going from the bulk crystal to the monolayer, the minimum at Σ shifts upwards. Finally, in the monolayer, the K-valley becomes the conduction band minimum. Consequently, the monolayer exhibits a direct band gap, and thus a different optical behavior [Zha13].

2.3 Vibrational modes

Figure 5 shows the in-plane phonon dispersions of WS_2 and WSe_2. The dispersion relations are qualitatively very similar. Quantitatively, the vibrational energy of the phonon modes is lower for WSe_2. This is due to the higher mass of selenium compared to sulfur.

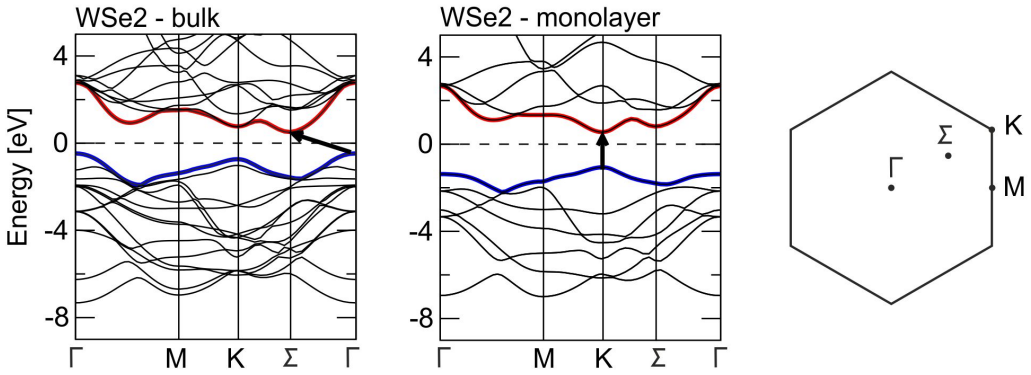

Figure 4: Electronic band structure of bulk and monolayer WSe_2. The valence band maximum and the conduction band minimum are highlighted in blue and red, respectively. The band gap is indicated with an arrow. The band structures differ at the Σ point, where the conduction band minimum is significantly higher in the monolayer than in the bulk crystal. For this reason, the monolayer possesses a direct band gap. Modified from [Kum12].

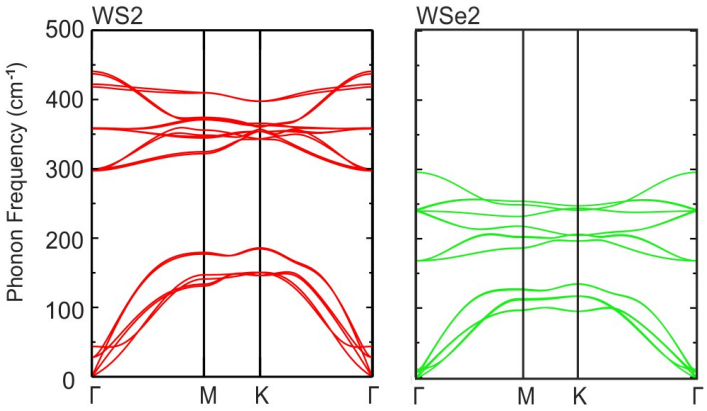

Figure 5: In-plane phonon dispersions of WS_2 and WSe_2. Data from [MS11] and [Sah13].

Additionally, multilayer structures also exhibit layer-breathing modes [Lui13] and shear modes [Tan12].

2.4 Vertical TMDC heterostructures

Vertical van der Waals heterostructures can be produced by either growing the two materials on top of each other or by mechanical stacking. The latter technique has the advantage that almost any rotation angle can be achieved.

2.4.1 Band alignment

The electronic behavior of a semiconductor heterojunction is determined to a large extent by the energetic position of their band gaps with respect to the vacuum level. Figure 6 (a) sketches the three different classes of band alignments. Figure 6 (b) shows the calculated band offsets for WSe_2 and WS_2. WS_2/WSe_2 heterostructures have type II band alignment. Since the chemical potentials of the two materials differ, charge is transferred across the interface when they are brought into contact. TMDCs have no dangling bonds

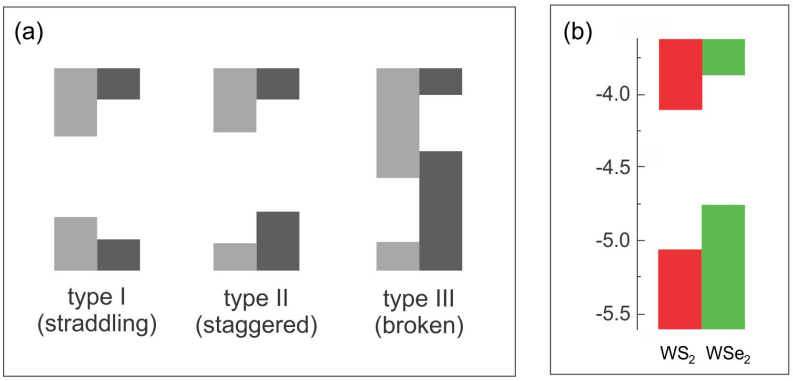

Figure 6: Panel (a) shows a scheme the three different kinds of heterojunctions. Gray areas stand for the valence and conduction bands of the two materials. Panel (b) shows the calculated band offsets for WSe_2 and WS_2, which form a type II heterojunction. Data from [Kan13].

at their surface and thus no chemical bonding occurs across the interface of TMDC heterostructures. Consequently, the band bending is well described by Anderson's rule (the electron affinity rule) [And62], [Chi16]. In the case of the WS_2/WSe_2 heterostructure, the chemical potential of WS_2 is lower. Hence, electrons flow from WSe_2 to WS_2 until a common chemical potential of both materials is established.

The charge separation leads to an electrostatic potential, which causes the band energy to depend on the position normal to the interface (band bending). A negative potential leads to a positive shift of the electronic energies, and vice versa. In the case of the WS_2/WSe_2 heterojunction, the bands of WS_2 are bent downwards and the bands of WSe_2 are bent upwards. However, for undoped wide band gap semiconductors, the number of thermally excited carriers is very low. Consequently, the total amount of surplus charge in the materials after contact is low as well. We estimated the resulting electrostatic potential for typical sample thicknesses (see Appendix C). The band bending is on the order of less than 5 meV (in the absence of defects, see discussion below). Consequently, the heterostructure samples examined in this work form a p-n-junction device. Figure 7 illustrates the bands and chemical potentials before and after contact.

Note that the band bending depends on the position of the chemical potential and thus on the doping level of the crystals. The crystals used in this work (purchased from hq graphene) are high-purity synthetic crystals with a low defect density. From the data given by the manufacturer, we know that WSe_2 is slightly p-doped while WS_2 is slightly n-doped. Apart from changing the chemical potentials and thus influencing the band alignment, defect states also increase the density of thermally excited carriers. Consequently, the enhance band bending effect. Nevertheless, we estimated that for the defect densities of these crystals, the band bending is still much lower than the band offsets between the materials. Hence, the p-n-character of the heterojunction is maintained even in the presence of low doping.

2.4.2 Dynamics of photoexcited type-II heterostructures

In p-n-heterojunctions such as the WS_2/WSe_2 heterostructure, after photoexcitation, charge separation across the interface occurs. This has an impact of the properties of the heterostructure: For example, the charge transfer quenches the photoluminescence peaks of the individual materials. A new peak at lower energy emerges, which corresponds to the interlayer exciton. The charge transfer has been observed for several TMDC hetero-

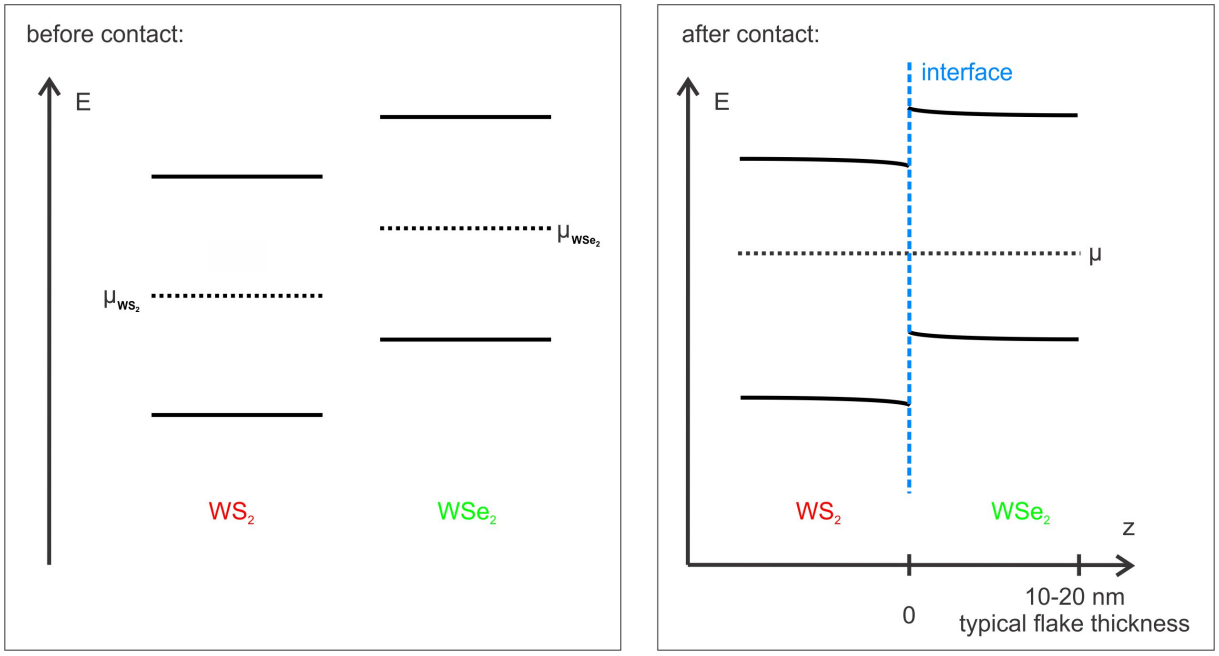

Figure 7: Band bending diagram for the undoped WSe_2/WS_2 heterojunction. Conduction band minimum and valence band maximum are displayed as solid lines, the chemical potentials are sketched as dashed lines. Upon contact, charge is transferred from WSe_2 to WS_2 until a common chemical potential is established. We assume undoped crystals. Due to the low amount of thermally excited carriers, the amount of band bending on the length scales of the sample is very low.

structures [Hon14], [Zhu15], [Che16], [Pan16] and it has been reported to occur on time scales below 50 fs [Hon14].

An important aspect for interfacial transfer is the existence of a momentum mismatch between the band edges of two materials. The momentum mismatch depends on the relative orientation of the two crystals. This is illustrated in Figure 8.

The momentum mismatch implies that a momentum transfer process has to occur before the (tightly bound) interlayer exciton is formed. It has been reported [Che16] that the formation of interlayer excitons occurs in two steps. This is depicted in Figure 9. In the first step, electrons transfer to higher-lying states in MoS_2. The charge transfer happens within 50 fs. In the second step, electrons relax to the conduction band minimum by transferring energy to the lattice. This step takes about 0.8-2 ps.

Apart from charge separation, there are other processes that contribute to the behavior of the system after excitation. The fastest of them is carrier-carrier scattering. The laser pulse initially excites a nonequilibrium distribution of excited carriers. The distribution depends on the photon energy. Carrier-carrier-scattering reestablishes a thermal energy distribution of the electronic subsystem, with temperatures that can reach several thousands of Kelvin. In our experiments on WS_2/WSe_2 heterostructures, mainly WSe_2 is excited. As explained in Section 2.2, the conduction band minimum of WSe_2 lies at the Σ point, whereas the direct band gap is located at the K-point. For excitations into the first excitonic resonance of WSe_2 (pump center wavelength 800 nm) the initial excited state population is created at the K-point. Then, electrons scatter to the lower-lying Σ-valley. Time- and angle-resolved photoemission experiments have shown that this takes less than 50 fs [Ber16]. In contrast, for excitation with a pump center wavelength of 400 nm, exited carriers are created at many points in the Brillouin zone of WSe_2. Also in this case, an

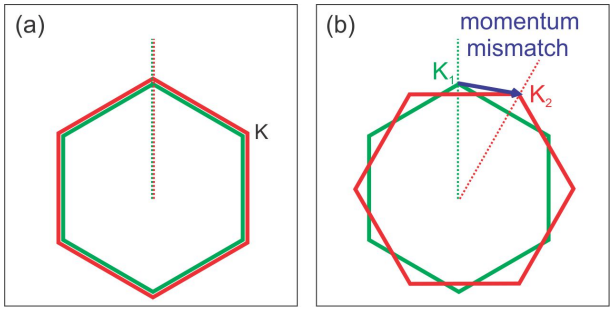

Figure 8: Panel (a) shows the Brillouin zones for aligned WS_2/WSe_2 heterostructures. Since the difference in lattice constants is small, there is almost no difference between the momenta of electrons at the K-points of the two materials. Panel (b) shows the Brillouin zones for heterostructures that are rotated relative to each other. The rotation in real space translates into a rotation in reciprocal space by the same angle. In contrast to the aligned heterostructure, there is a significant momentum difference between equivalent points in the Brillouin zone.

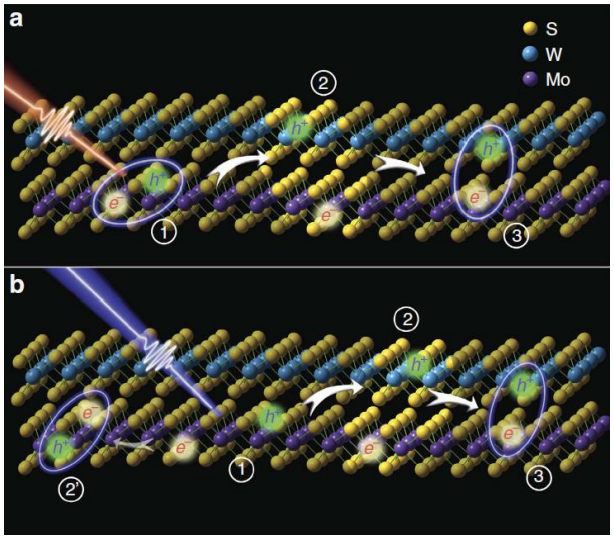

Figure 9: Formation steps of the charge transfer exciton, shown for the MoS_2/WS_2 heterostructure. Panel (a) shows a case in which WS_2 is excited at the excitonic resonance (1). In the first step of exciton formation, electrons transfer to MoS_2 (2). This transfer is possible since the energy of the electrons is well above the band gap, and thus states with matching energy and momentum are available. After this step, the carriers are weakly bound. Then, the electrons relax to the conduction band minimum of MoS_2 and form tightly bound interlayer excitons (3). Panel (b) shows a situation at higher photon energies, where free carriers are excited (1). The direct charge transfer (2) has been shown to be much faster than the formation of tightly bound intralayer excitons (2'). From [Che16].

electron distribution with most electrons in the Σ valley is established quickly (within a time scale of around 100 fs [Pup]). Compared to 800 nm excitation, the electronic temperature is much higher because of the initial excitation of electrons into states well above the band gap.

Carrier-carrier scattering only redistributes energy between the electrons, but the total energy of the electronic subsystem remains unchanged. Equilibration between hot carriers and the lattice is achieved via carrier-phonon coupling, which leads to a cooling of the electronic subsystem by the creation of phonons. The time scale of carrier-lattice equilibration within one material is typically on the order of few picoseconds. For WSe_2 and 800 nm excitation, depending on the pump laser fluence, time constants of 1.5-4 ps are observed. For 400 nm excitation (and thus much higher electronic temperatures), a fluence-independent time constant of around 1 ps is observed [Ber].

In general, carrier-phonon scattering produces a nonequilibrium phonon distribution, which is governed by the matrix elements for carrier-phonon scattering. Thermalization of the lattice is achieved via phonon-phonon scattering. Phonon-phonon scattering is mediated by the anharmonicities in the interatomic potentials. Typically, it is a rather slow process compared to carrier-carrier and carrier-phonon scattering. For WSe_2, time-resolved diffraction experiments have shown that phonon-phonon equilibration takes several tens of picoseconds [Wal17].

In the case of heterostructure samples, vibrational coupling across the interface can also contribute to the equilibration of the system. The conductance of an interface (also called Kapitza conductance) can be described using the diffuse mismatch model[1] [Swa89]. In this model, the phonons are assumed to scatter from a state on one side of the interface into a state on the other side. The phonon transfer rate is then determined by the overlap of the phonon dispersions of the two materials. This depends on the relative alignment of the two materials, since the real-space rotation angle between them translates into a rotation of the two Brillouin zones by the same angle (compare Figure 8). In general, it should be significantly slower than phonon-phonon equilibration in the individual materials, that is slower than tens of picoseconds.

The interplay of all the equilibration processes described above determines the relaxation pathway of the system. With our experiments, we are able to measure the transient phonon population and thus the structural dynamics of the sample. Consequently, we can draw conclusions on processes that involve changes in the energy content of the lattice. Before discussing the results, the next sections will give an introduction to high-energy electron diffraction. The focus lies particularly on the diffraction patterns of thin films and heterostructures and on the signatures of phonons in diffraction.

[1] Except for very low temperatures below 1 K, where the acoustic mismatch model provides a better description.

3 Femtosecond electron diffraction

In a diffraction experiment, light or matter waves are sent to a sample and interact with it, leading to scattering of the waves. The intensity of the scattered light or particles contains information about the structure of the sample and is recorded and analyzed. The interaction of the beam with a sample depends on the type of radiation used: X-rays, for example, interact mostly with the electron cloud surrounding the atoms while neutrons interact with the magnetic moments present in the sample. In contrast to X-rays and neutrons, electrons are charged particles. Therefore, they interact with the electrostatic potential of the sample. Even though the diffraction patterns obtained by the different techniques differ, they all probe the structural order of the sample.

While static diffraction measurements yield information on the structure of the sample in equilibrium, a pump-probe-scheme can be applied to obtain information on the structural dynamics of the sample after excitation. In a pump-probe diffraction experiment, first a pump pulse is sent to the sample to excite it. Secondly, a probe pulse (here: a bunch of electrons), is used to probe the state of the lattice. By varying the time delay between the two pulses, the evolution of the lattice structure after excitation can be measured.

In both static and time-resolved diffraction, the interpretation of the diffraction patterns is usually not straightforward. For example, diffraction patterns depend on the amount of secondary scattering and on contributions of inelastic scattering. In the case of high-energy transmission electron diffraction of thin films, the probability to find an electron deflected is usually lower than the probability that it is measured in the (000) beam. Furthermore, the number of inelastic scattering events is very low. The following sections are therefore dedicated to diffraction theory in this limit.

3.1 Kinematic diffraction theory

In general, classical diffraction theory describes the scattering using the Huygens-Fresnel principle: when the incident wave hits the sample, each diffraction center - this is, each point where the diffraction potential is non-zero - gives rise to a spherical wave . This wave has the same frequency as the incident wave and its amplitude is proportional to the amplitude of the incident beam at that point. The coherent superposition of all the outgoing spherical waves determines the diffraction pattern.

In particular, kinematic diffraction theory describes the limit of very low total scattering, that is a situation where most of the incident beam is left unaffected by the scattering potential. The approximation made in kinematic diffraction theory is that at any point in the sample, the total incident intensity is the same as it was before hitting the sample. In other words, secondary diffraction of the outgoing spherical waves and attenuation of the incident beam are not considered. In this limit, it can be shown (see for example [Iba09]) that the diffracted amplitude A_{diff} is given by the Fourier transform of the diffraction potential $V(\mathbf{r})$:

$$A_{\text{scatt}}(\mathbf{k}-\mathbf{k_0}) \propto \exp\{-i\omega_0 t\} \int V(\mathbf{r}) \exp\{i(\mathbf{k}-\mathbf{k_0})\cdot\mathbf{r}\} d\mathbf{r} \tag{1}$$

Here, $\mathbf{k_0}$ and $\mathbf{k}$ denote the wave vectors of the incident and outgoing waves, respectively.

Even in a situation where secondary scattering plays a role, the results of kinematic scattering theory often describe the geometry of the diffraction pattern well. Typically, only the intensities differ. In the following, we use mainly kinematic scattering theory to discuss diffraction by thin crystalline films and heterostructures.

3.2 Diffraction by crystals

3.2.1 The Fourier transform of periodic structures

To describe the periodicity of a crystal, the Bravais lattice concept can be used. A Bravais lattice is a periodic set of points in space spanned by so-called primitive vectors (one for each dimension). It describes the periodicity of the unit cell.

To complete the description of the periodic structure, also the distribution inside the unit cell is needed. As discussed above, in the case of electron diffraction, the electrostatic potential is the relevant quantity. It consists of the electrostatic potential of the individual atoms in the unit cell plus a contribution from the chemical bonds:

$$V_{\text{scatt}} = V_{\text{atom}} + V_{\text{chem}} \tag{2}$$

However, the contribution from bonding is typically smaller than 1% [Pen10] and may therefore be neglected for most purposes (isolated atom superposition approximation). In this approximation, it is possible to write the potential in the unit cell as follows:

$$V_{\text{scatt}}(\mathbf{r}) \approx V_{\text{atom}}(\mathbf{r}) = \sum_{i=1}^{n} V_i(\mathbf{r} - \mathbf{r}_i) \tag{3}$$

Here, the V_i are the individual atomic electrostatic potentials and the $\mathbf{r}_i$ refer to the positions of the n atoms in the unit cell. Finally, the periodic potential of the crystal is obtained by convoluting the Bravais lattice with the potential distribution inside the unit cell.

As shown in Section 3.1, to determine the diffraction pattern, we have to compute the Fourier transform of the electrostatic potential. The Fourier transform of a convolution of two functions is the product of their Fourier transforms. Using this and the linearity of the Fourier transform, the scattered amplitude can be written as:

$$A_{\text{scatt}}(\mathbf{k} - \mathbf{k_0}) \propto \mathbf{R}(\mathbf{k} - \mathbf{k_0}) \cdot \sum_{\mathbf{i=1}}^{\mathbf{n}} \mathrm{f_i}(\mathbf{k} - \mathbf{k_0}) \exp\{i\, \mathbf{r_i} \cdot (\mathbf{k} - \mathbf{k_0})\} \tag{4}$$

Here the $\mathrm{f}_i = \int_{\text{unit cell}} V_i(\mathbf{r}) \exp\{i(\mathbf{k} - \mathbf{k_0}) \cdot \mathbf{r}\} d\mathbf{r}$ are the atomic scattering factors. R denotes the Fourier transform of the Bravais lattice, the reciprocal lattice:

$$R(\mathbf{q}) = \begin{cases} 1 & \text{if } \mathbf{q} = \mathbf{G} \\ 0 & \text{otherwise} \end{cases} \tag{5}$$

Here, $\mathbf{G} = \sum n_i \mathbf{b_i}$ is a reciprocal lattice vector. The $\mathbf{b_i}$ are the primitive vectors of the reciprocal lattice. They are related to the primitive vectors of the Bravais lattice $\mathbf{a}_i$ as follows (see for example [Kit05]):

$$\mathbf{b}_i = 2\pi \frac{\mathbf{a}_j \times \mathbf{a}_k}{\mathbf{a}_i \cdot (\mathbf{a}_j \times \mathbf{a}_k)} \tag{6}$$

According to Equations 4 and 5, the scattered intensity is zero unless the difference between the incoming and the outgoing wavevector corresponds to a reciprocal lattice vector:

$$\mathbf{k} - \mathbf{k_0} = \mathbf{G} \tag{7}$$

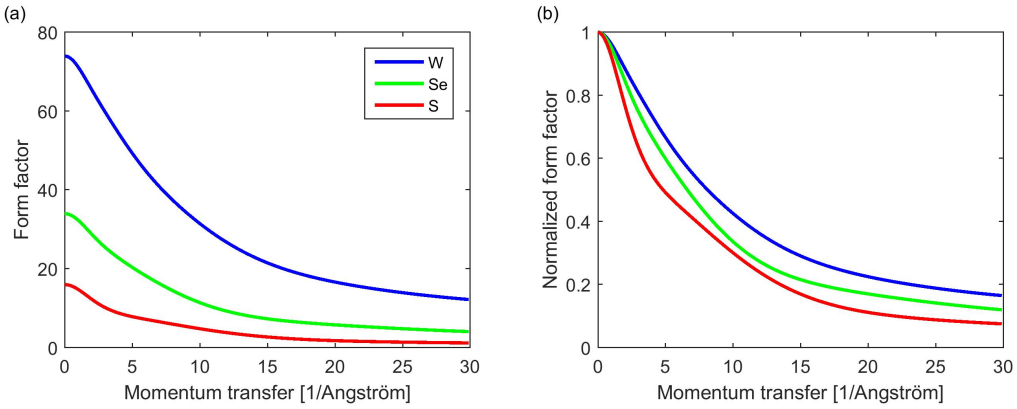

Figure 10: Panel (a) shows the form factors of tungsten, selenium and sulfur. Panel (b) shows the normalized form factors. Their dependence on the scattering angle is very similar for all the materials. Consequently, the contribution of the individual atoms to the total peak intensity is similar for all diffraction orders. Data from [Bro06].

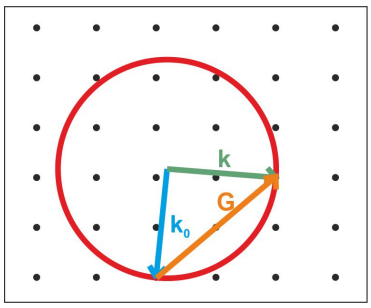

Figure 11: Scheme of the Ewald sphere construction in two dimensions. The wavevector $\mathbf{k_0}$ of the incoming wave is drawn such that it ends on a point of the reciprocal lattice. The wavevectors of elastically scattered electrons lie on a circle with radius $|\mathbf{k_0}|$ around this point. The diffraction condition $\mathbf{k} - \mathbf{k_0} = \mathbf{G}$ is fulfilled if the circle coincides with a point of the reciprocal lattice.

In other words, this means that the reciprocal lattice of a structure determines the position of the diffraction peaks. On the other hand, their intensity is governed by the second multiplicand of Equation 4, the so-called structure factor:

$$F_{\mathbf{G}} = \sum_{i=1}^{n} \mathrm{f}_i(\mathbf{G}) \exp\{i\, \mathbf{r}_i \cdot \mathbf{G}\} \tag{8}$$

Figure 10 displays the form factors $f_i(\mathbf{G})$ of the materials studied in this work.

3.2.2 The Ewald sphere

As shown in the previous section, in order for the scattered intensity in a certain direction to be non-zero, the scattering condition (Equation 7) has to be fulfilled. This condition can be visualized using a geometric construction, the Ewald sphere (see Figure 11).

Even for large wavevectors, as it is typically the case in high-energy electron diffraction, the diffraction condition is almost never (exactly) fulfilled. However, so far, we have not taken into account the finite size of the crystal. This will be discussed in the following section.

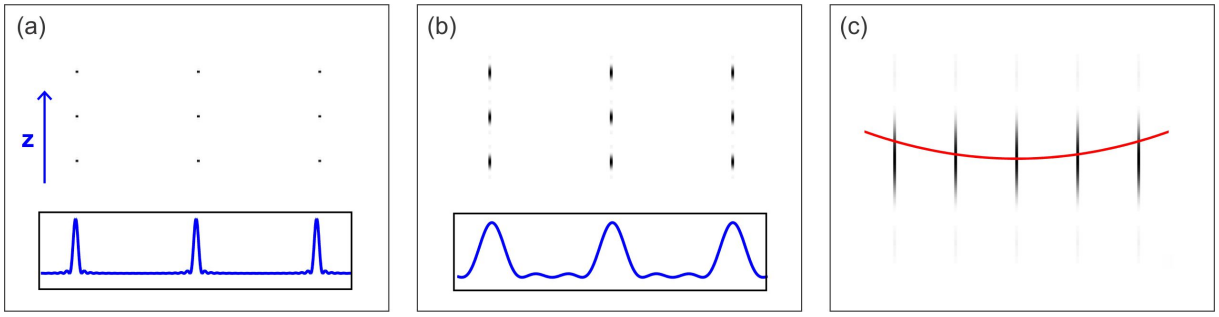

Figure 12: Reciprocal lattice of a thin film consisting of (a) 20 monolayers and (b) 4 monolayers. In blue, a line profile in z-direction is shown. The finite size leads to a softening of the diffraction condition in z. Panel (c) shows a typical Ewald sphere construction for high-energy electron diffraction. In this particular example, we assume 20 monolayers, the lattice constant of graphite and 60 keV electron energy. The image is stretched in z to make the finite-size effect visible.

3.2.3 Diffraction by thin films

In order to describe a finite crystal, the periodic potential has to be multiplied by a window function. In the case of thin films, the crystal is quasi-infinite in two dimensions but finite in the third one. Therefore, the scattering potential has to be multiplied by a slit function in this direction. In the Fourier transform, this translates into a convolution of Equation 4 with a Sinc function (the Fourier transform of a slit function). Figure 12 illustrates the effect for a two-dimensional crystal and different crystal thicknesses in z-direction.

The finite size leads to a softening of the diffraction condition in the corresponding direction in reciprocal space. Nevertheless, for multilayer samples, the softening of the diffraction condition is still quite small compared to the lattice constant. On the other hand, the curvature of the Ewald sphere is very low. Furthermore, in our experiment, additional softening of the diffraction condition comes from the fact that the electrons can have slightly different energies and/or directions. Due to the combination of these effects, many reciprocal lattice spots of the same plane contribute to the diffraction pattern. The Bragg peak intensity decreases with increasing distance from the (000) point[2]. Consequently, at normal incidence, the positions of the diffraction spots correspond to the in-plane reciprocal lattice of the TMDCs.

3.2.4 Diffraction by heterostructures

A vertical heterostructure can be formally described by a sum of the two periodic potentials, each of them multiplied by the appropriate rectangular window function. Due to the linearity of the Fourier transform, the Fourier transform of the heterostructure, and thus the diffraction pattern in the kinematic approximation, is the sum of the reciprocal lattices of the two films. However, additional diffraction spots (so-called extraordinary spots) are observed frequently [Cha01]. These spots are not described by kinematic diffraction theory, because they stem from secondary scattering. The location of these spots is given by the convolution of the two reciprocal lattices [Bas64]. Figure 13 illustrates secondary-scattering effects for two simple one-dimensional crystals.

[2]In our experiments, only the zero order Laue zone (ZOLZ) is observed, the (hk0) spots. For larger scattering vectors, the Ewald sphere eventually matches reciprocal lattice points (hkl) with $l \neq 0$ (higher order Laue zones, HOLZ). Their intensity can be high.

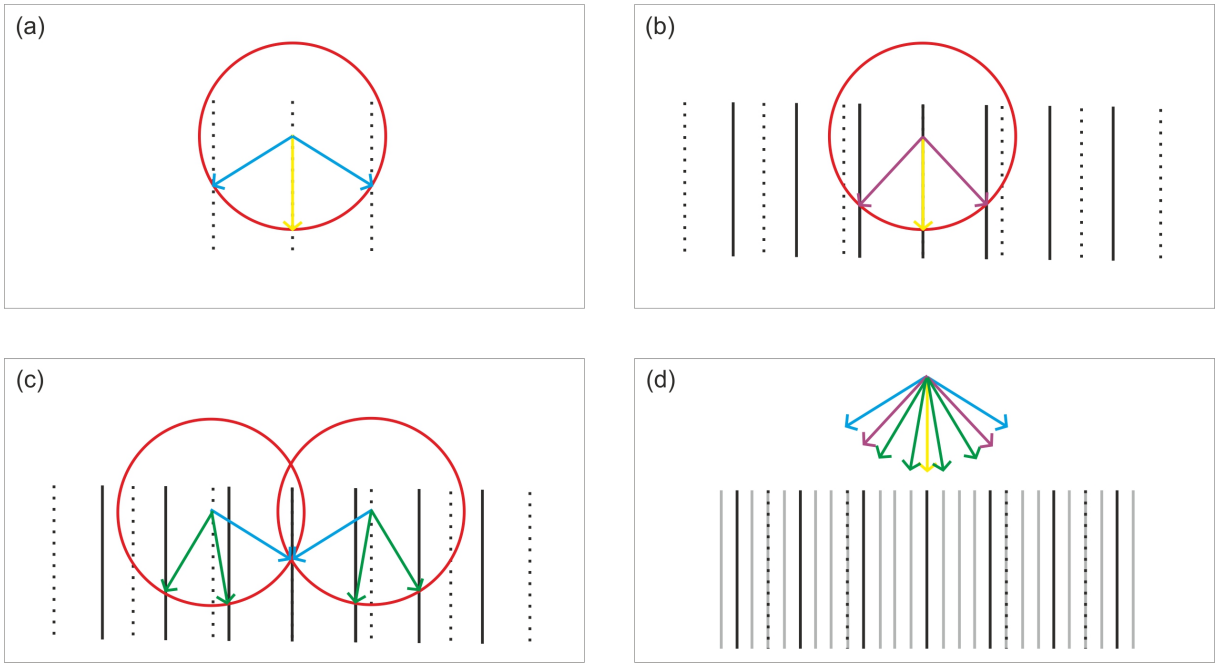

Figure 13: Formation of extraordinary spots due to secondary diffraction. Panel (a) shows the Ewald sphere construction (red) for scattering in the first thin film, the reciprocal lattice of which is shown as dotted rods. For simplicity, the curvature of the Ewald sphere is exaggerated. The incoming/zero-order beam is shown in yellow, diffracted beams in blue. Panel (b) shows the Ewald sphere construction for the kinematic diffraction taking place in the second film. The reciprocal lattice of the second film is shown as solid black lines, diffracted beams are shown in purple. Panel (c) shows the Ewald sphere construction for secondary scattering, that is scattering of the higher-order beams of material 1 (blue). The outgoing beams are shown in green., Panel (d) shows all the outgoing beams and relates them to the convolution of the reciprocal lattices (gray lines). Within the kinematic theory, scattering spots always correspond to one of the individual reciprocal lattices (purple and blue beams). Secondary diffraction (green beams) leads to spots that appear at sites corresponding to the convolution of both lattices.

3.3 The role of phonons in diffraction

So far, we have regarded the crystal as being static and perfectly periodic. However, in reality thermal vibrations cause the atomic positions to fluctuate. On average, the atomic motion corresponds to an effective smoothing of the potential. Hence, it leads to a decrease of Bragg peak intensity. At the same time, the diffuse scattering background increases.

The decrease of Bragg peak intensity can be described by including the atomic displacements in the structure factor, which then becomes time-dependent:

$$F(\mathbf{G},t) = \sum_{i=1}^{n} \mathrm{f}_i(\mathbf{G}) \exp\{i\,(\mathbf{r}_i + \mathbf{u}_i(t)) \cdot \mathbf{G}\} \tag{9}$$

Here, $\mathbf{u}_i(t)$ denotes the displacement of the i-th atom in the unit cell[3].

The time average of the structure factor is given by:

$$\langle F(\mathbf{G},t)\rangle_t = \sum_{i=1}^{n} \mathrm{f}_i(\mathbf{G}) \exp\{i\,\mathbf{r}_i \cdot \mathbf{G}\} \langle \exp\{i\,\mathbf{u}_i(t) \cdot \mathbf{G}\}\rangle_t \tag{10}$$

$$\approx \sum_{i=1}^{n} \mathrm{f}_i(\mathbf{G}) \exp\{i\,\mathbf{r}_i \cdot \mathbf{G}\} \exp\{-\frac{1}{2} \langle (\mathbf{u}_i(t) \cdot \mathbf{G})^2\rangle_t\} \tag{11}$$

The last equality holds within the harmonic approximation. The attenuation depends on the square of the scalar product between the reciprocal lattice vector and the lattice displacement. For normal incidence of the beam and ZOLZ diffraction as in our experiment, this means that the diffraction peak intensity is only sensitive to in-plane atomic displacements. If the mean displacement is isotropic, Equation 11 can be further simplified to give:

$$\langle F(\mathbf{G},t)\rangle_t = \sum_{i=1}^{n} \mathrm{f}_i(\mathbf{G}) \exp\{i\,\mathbf{r}_i \cdot \mathbf{G}\} \exp\{-\frac{1}{6} \langle u_i^2\rangle_t G^2\} \tag{12}$$

The factor $\exp\{-\frac{1}{6} \langle u_i^2\rangle_t G^2\}$ is called the temperature factor and is often written as:

$$\exp\{-\frac{1}{6} \langle u_i^2\rangle_t G^2\} = \exp\{-B_k s^2\} \tag{13}$$

with $s = \frac{G}{4\pi}$ and $B_k = \frac{8}{3}\pi^2 \langle u_i^2\rangle$. B_k is called the Debye-Waller factor. Note that for layered materials such as the TMDCs examined in this work, which are very anisotropic materials, Equations 12 and 13 cannot be used. However, in this case, an in-plane and out-of-plane Debye-Waller factor can be defined.

The Debye-Waller factor is a quantity describing the mean squared displacement $\langle u_i^2\rangle$, which is the result of all the phonons present in the sample. For thermal phonon distributions, the mean squared displacement can be related to the temperature. In the case of a crystal with only one atom per unit cell, it can be calculated based on the phonon dispersion. However, in the case of crystals with several atoms per unit cell, such as TMDCs, additional knowledge of the phonon polarization vector for each mode and each atom of the unit cell is necessary. In the following, we outline the treatment of crystals with one atom per unit cell given in reference [Pen10]. It allows to illustrate some general relations that are also valid for more complex crystals.

[3]Correlations of the atomic motions are not taken into account, which is valid for the calculation of the Bragg peak attenuation (see for example [War90])

In general, the displacement $\mathbf{u}$ of an atom can be written as the sum over the contributions of all phonon modes:

$$\mathbf{u} = \sum_{\mathbf{q},j} \mathbf{u}(\mathbf{q}, j) \tag{14}$$

$\mathbf{q}$ is the phonon momentum, j is an index labeling the phonon modes (here: 3). The contribution of one phonon mode, $\mathbf{u}_{\mathbf{q},j}$, can be written as:

$$\mathbf{u} = a_{\mathbf{q},j}\, \mathbf{e}_{\mathbf{q},j} \cos\{\omega_{\mathbf{q},j} t - \mathbf{q}\cdot\mathbf{r} - \phi_{\mathbf{q},j}\} \tag{15}$$

$a_{\mathbf{q},j}$ is the amplitude of the mode, $\mathbf{e}_{\mathbf{q},j}$ its polarization vector, $\omega_{\mathbf{q},j}$ its frequency, $\phi_{\mathbf{q},j}$ is an arbitrary phase and $\mathbf{r}$ is the position of the atom. In the next step, the amplitude of each modes is related to the total energy stored in the respective mode. For this, we calculate the total mean kinetic energy of the lattice, which corresponds to half of the total energy of the lattice[4].

$$\langle E_{\mathrm{kin}} \rangle = \frac{1}{2} \sum_{l} m \left\langle \left(\frac{\partial \mathbf{u}_l}{\partial t}\right)^2 \right\rangle = \frac{1}{4} mN \sum_{\mathbf{q},j} a_{\mathbf{q},j}^2 \omega_{\mathbf{q},j}^2 \tag{16}$$

m is the atomic mass and N is the number of atoms in the crystal. On the other hand, the total energy of the lattice $\langle E_{\mathrm{tot}} \rangle$ can be written as a sum over all the contributions of the different phonon modes:

$$\langle E_{\mathrm{tot}} \rangle = \sum_{\mathbf{q},j} \langle E_{\mathbf{q},j} \rangle \tag{17}$$

Combining Equations 16 and 17, the following relation for the amplitude is obtained:

$$a_{\mathbf{q},j}^2 = \frac{2 \langle E_{\mathbf{q},j} \rangle}{mN\omega_{\mathbf{q},j}^2} \tag{18}$$

On the other hand, the mean energy of one phonon mode in thermal equilibrium is given by:

$$\langle E_{\mathbf{q},j} \rangle = \hbar\omega_{\mathbf{q},j} (\langle n_{\mathbf{q},j} \rangle + \frac{1}{2}) \tag{19}$$

with the average occupation number $\langle n_{\mathbf{q},j} \rangle$ of a phonon mode, according to Bose-Einstein statistics, given by:

$$\langle n_{\mathbf{q},j} \rangle = \frac{1}{\exp\{\frac{\hbar\omega_{\mathbf{q},j}}{kT}\} - 1} \tag{20}$$

Finally, the total mean squared displacement of an atom in the crystal can be calculated:

$$\langle \mathbf{u^2} \rangle = \frac{1}{2} \sum_{\mathbf{q},j} a_{\mathbf{q},j}^2 = \frac{\hbar(\langle n_{\mathbf{q},j} \rangle + \frac{1}{2})}{mN\omega_{\mathbf{q},j}} \tag{21}$$

A very important result is that the total mean squared displacement depends inversely on the phonon frequency. Consequently, acoustic phonon modes contribute much more to the Bragg peak attenuation than optical modes. Note that this is not an occupation effect, but that the contribution *per phonon* depends on the phonon frequency. Furthermore, the result also allows to draw qualitative conclusions on the Debye-Waller-factors of more the more complex materials studied in this work: Comparing the phonon dispersions of WSe_2 and WS_2 (Figure 5), it can be seen the phonon modes of WSe_2 have on average

[4]This statement holds for an harmonic oscillator in general. Since each phonon mode is an (uncoupled) harmonic oscillator, the relation also holds for the total mean kinetic energy of the lattice.

lower phonon frequencies than WS_2. Consequently, a significantly higher Debye-Waller factor is expected for WSe_2.

The second relevant quantity in Equation 21 is the mean occupation number $\langle n_{\mathbf{q},j} \rangle$, which is changed transiently in a time-resolved diffraction experiment. Note that after the lattice has reached a thermal phonon distribution, the occupation number also depends on the frequency (compare Equation 20). Consequently, in equilibrium, high-frequency phonons contribute even less to the total Debye-Waller-effect because they are less populated.

To summarize, time-resolved diffraction experiments probe the phonon population, but with a higher sensitivity for low-frequency modes. The main observable, the attenuation of the Bragg peak intensity, depends on the phonon properties. Therefore, the magnitude of the Debye-Waller effect varies for different materials.

Another effect that has to be kept in mind in electron diffraction, especially when performing experiments on heterostructures, is the attenuation of the zero-order beam. In Equations 11 and 12, the Bragg peak attenuation strongly depends on the magnitude of the scattering vector. For the zero-order peak ($G = 0$), no attenuation is predicted. Nevertheless, in reality, the zero-order intensity is often affected by the lattice temperature, albeit much less than the higher orders [Lig11], [Boe64]. The effect increases with increasing sample thickness. The peak attenuation including zero-order effects can be well described by the following empirical formula [Lig11]:

$$\frac{I(\mathbf{G}, T)}{I(\mathbf{G}, T_{\mathrm{ref}})} = \exp\{-(b + a \cdot G^2) \cdot (T - T_{\mathrm{ref}})\} \tag{22}$$

Here, T_{ref} is the reference temperature, usually room temperature, a is a material-dependent parameter related to the Debye-Waller factor and b depends on the material as well as on the sample thickness.

The underlying reason for the zero-order attenuation is secondary scattering. With increasing thickness, the amount of secondary scattering in the material increases as well. As a consequence, a part of the scattered beam is scattered back to the (000) spot. Figure 14 illustrates the process using an Ewald sphere construction, conceptually similar to Figure 13.

So far, we have described the intensity loss of the Bragg diffraction spots. Since the total intensity is conserved, the intensity has to rise elsewhere: the diffuse background of the diffraction image increases. A treatment of this effect can be found in [Xu05]. To first order, a phonon mode with momentum $\mathbf{q}$ leads to additional intensity at $\mathbf{q} + \mathbf{G}$ (with $\mathbf{G}$ being any of the reciprocal lattice vectors). Consequently, the diffuse scattering background contains information about the phonon momenta. In time-resolved measurements, this can be exploited to learn about the transient distribution of phonon momenta. Compared to the Debye-Waller-analysis, this allows to study the coupling of excited carriers to specific phonon modes in greater detail.

Apart from incoherent vibrations, it is known that electronic excitation of crystals with femtosecond laser pulses can also lead to the excitation of coherent phonons. Their effect on the diffraction image depends on the direction and symmetry of the lattice distortion caused by the coherent phonon. In principle, coherent phonons can be observed as oscillatory changes. In our case, however, the oscillation period of the coherent phonons that are excited is shorter than the time resolution of our setup. In consequence, we essentially observe the time-average of the effects. We simulated the effect of the A_{1g} and E_{2g} coherent phonons on the diffraction pattern using CrystalMaker®. Especially

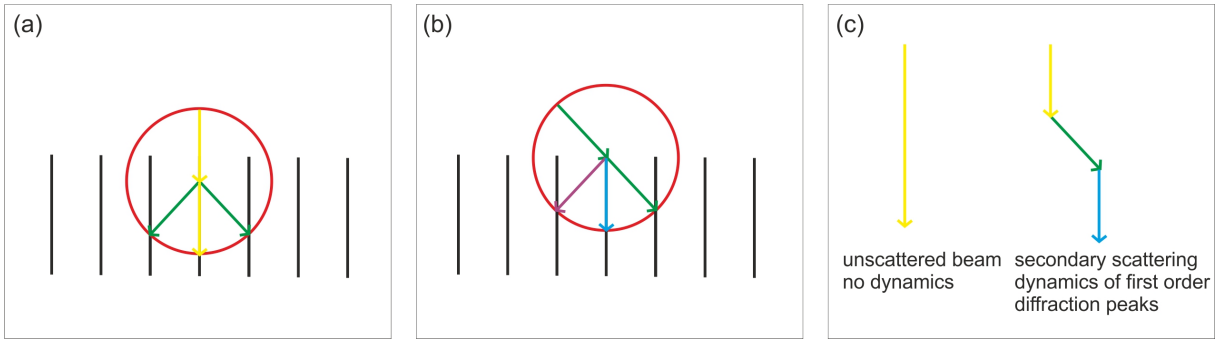

Figure 14: Ewald sphere construction of the mechanism leading to zero-order effects. Panel (a) shows primary scattering. Panel (b) shows secondary scattering of a first order beam. A part of the beam is scattered back to the zero order (blue). Panel (c) shows two different contributions to the (000) spot. The unscattered beam (yellow) is not attenuated by phonons. In contrast, the secondary scattered beam is attenuated like a first order beam. Consequently, in total, the zero order is attenuated. The more pronounced secondary scattering becomes, that is the thicker the sample is, the larger is the zero-order effect.

the E_{2g} mode causes momentary changes in the diffraction pattern[5]. However, after time-averaging, the effect vanishes. Consequently, we don't expect to observe any trace of coherent phonons in the diffraction images.

In conclusion, femtosecond electron diffraction allows to observe pump-induced changes in the (incoherent) phonon population. Two observables indicate the amount of phonons present in the crystal: the Bragg peak intensity and the amount of inelastic scattering background. In the following, we analyze the response of the Bragg peak intensity to photoexcitation. It should be kept in mind that the experiments are more sensitive to low-frequency phonons. Additionally, at normal incidence, only in-plane displacements can be observed.

[5]The simulations were performed at normal incidence. It is reasonable that the E_{2g} mode affects the diffraction image considerably in this geometry since in this case the distortions are perpendicular to the incident beam.

4 Experimental techniques

4.1 The femtosecond electron diffraction setup

Figure 15 shows a sketch of the experimental setup. A Ti:Sa amplifier is used to produce short laser pulses with a center wavelength of 800 nm and a pulse duration of around 30 fs at a repetition rate of 1.1 kHz. The beam is split into a probe and a pump beam. The probe beam is sent into a non-collinear optical parametric amplifier (NOPA) to produce light with a photon energy of 2.2 eV (565 nm). This energy corresponds to half of the work function of the gold photocathode (~ 4.4 eV). The output of the NOPA is compressed to reach a pulse duration of 30-40 fs and then focused onto the photocathode, where it leads to the creation of multiple electrons (several thousands per pulse) via a two-photon process. The emitted electrons are accelerated and directed to the sample, where they diffract. Diffraction images are recorded in transmission using a phosphor screen and a camera. For focusing of the electrons, a magnetic lens is used. It can be operated in diffraction and imaging mode, the latter allowing a precise positioning of the sample.

Since electrons have a quadratic dispersion relation, the wavepackets describing single electrons broaden during propagation. For multiple-electron pulses, space charge effects lead to further pulse broadening. Since this decreases the time resolution, the total propagation distance of the electrons to the sample is kept as short as possible. At 60 keV electron energy, a time resolution of ~250 fs is achieved.

The pump beam goes through a delay stage to adjust the time delay between the pump and probe pulses. Optionally, the 800 nm pump pulses can be frequency-doubled using a BBO crystal. The pump beam is then sent into the chamber, where it hits the sample from the back side.

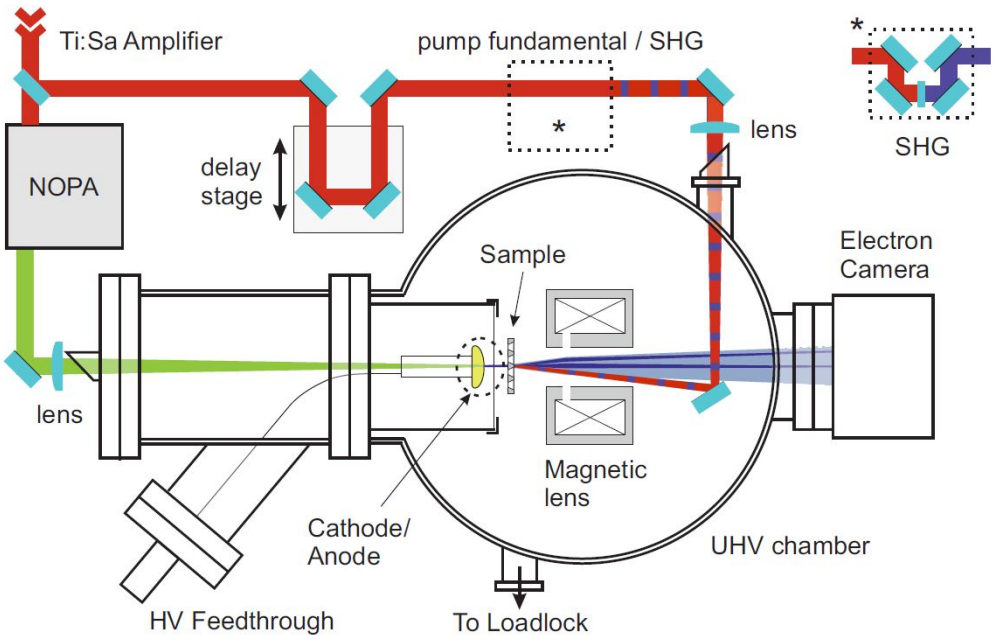

Figure 15: The femtosecond diffraction setup (see text for details). From [Wal16b].

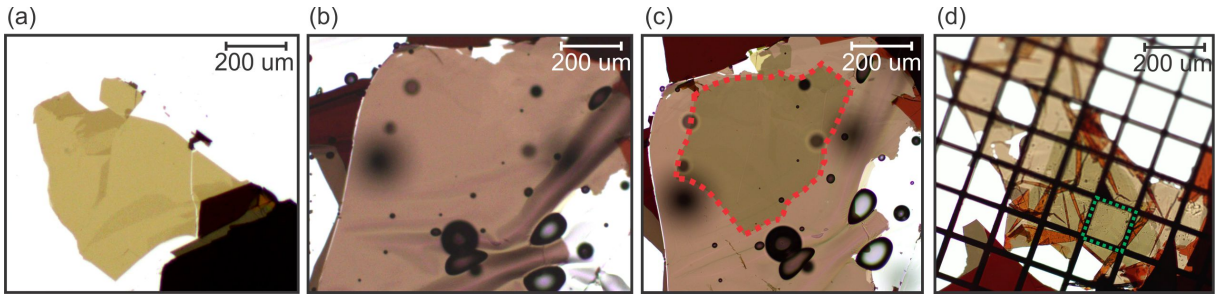

Figure 16: Different steps of the sample preparation. Panel (a) shows a WS_2 flake on PDMS. Panel (b) shows a WSe_2 flake on Crystalbond. The dark circles are air bubbles enclosed in the Crystalbond glue. Panel (c) shows the WS_2/WSe_2 heterostructure on Crystalbond (marked in red). Panel (d) shows the heterostructure after transfer onto a TEM grid. The sample shown here is sample number 1 (see Appendix B for details). The dotted green line marks the spot where the measurements were taken.

4.2 Sample preparation

The heterostructure samples are prepared using the viscoelastic stamping technique [CG14]. For the PDMS stamp we use Sylgard® 184 Silicone Elastomer from Dow Corning. Instead of mixing 1 part of curing agent with 10 parts of the uncured product (by weight) as suggested by the manufacturer, we use a 1:13 ratio to increase the stickiness of the elastomer. We fabricate rather thick PDMS sheets with thicknesses of about 2-3 mm. The reason is that thick stamps seem to decrease the risk of cracks during the fabrication process. TMDC flakes are deposited on the PDMS stamp by the following procedure:

1. The stamp is placed on top of a bulk crystal (a pre-thinned, but still non-transparent, thick flake attached to a glass slide with tape). It is extremely important to choose a crystal with shiny, undamaged surfaces in order to get large flakes. During this step, caution has to be taken to apply only very little or no pressure. Otherwise, the crystal is damaged, which results in shattered, small flakes.

2. The stamp is left on top of the crystal for some time (around 20s is sufficient) in order to allow the PDMS to adhere to the sample. This is related to the viscoelasticity of PDMS: it behaves solid-like on short time scales but like a liquid on long time scales. Consequently, if given the time, it can adhere very well and homogeneously to the crystal surface.

3. The stamp is removed quickly from the crystal. Here it is important to bend the stamp as little as possible to avoid cracks. The stamp is placed on a glass slide and suitably large and thin flakes are identified using the optical microscope.

Figure 16 a shows an example for a flake obtained by this technique. To produce the second part of the heterostructure, we use a water-soluble mounting adhesive (Crystalbond 555 from SPI® supplies). We heat a piece of Crystalbond on a glass slide to around 150°. To get flakes onto the melted crystal bond, we use thick flakes on Scotch tape. The Scotch tape is attached to a piece of PDMS on a glass slide. It is placed on top of the liquid Crystalbond. After cooling, the Crystalbond becomes solid again. Then, the glass slide with the thick crystal is removed, leaving some flakes attached to the Crystalbond. They are thinned by mechanical exfoliation until reaching the desired thickness. Figure 16 (b) shows a WSe_2 flake obtained in this way.

In the next step, the two parts of the heterostructure are brought into van der Waals contact and the PDMS stamp is slowly removed. The piece of Crystalbond with the heterostructure is cut out and floated on the surface of distilled water. The water-soluble Crystalbond slowly dissolves, leaving the heterostructure floating on the surface. From there, it can be picked up with the TEM grid. Figure 16 (d) shows the finished sample.

For AFM and optical measurements, TMDC flakes were brought on glass and fused silica substrates using the following procedure:

1. Similar to above, flakes are glued to a glass substrate using a mounting adhesive. However, in this case we use Crystalbond 509, which is soluble in acetone, due to its superior solubility. The flakes are thinned until reaching the desired thickness.

2. The piece of glue containing the flake is cut out and placed onto the desired substrate.

3. The glue is dissolved by carefully dropping small quantities of acetone onto it using a syringe. A tissue or cotton swab is used to absorb the acetone with the dissolved glue on the side of the substrate. Several cycles of dropping acetone and removing it are necessary to ensure that as little glue as possible is left on the sample.

4.3 Thickness and optical properties of multilayer flakes

For the interpretation of the pump-probe-experiments, it is important to know the thickness of the flakes and the penetration depth of the laser pulse into the sample. There are methods to measure the thickness of flakes with a small number of layers, e.g. using the dependence of certain Raman peaks on the number of layers. However, these methods are not applicable to the samples used in our experiments, in which each material is more than 10 layers thick. In principle, atomic force microscopy (AFM) can be used to measure the thickness of such flakes. Nevertheless, apart from being time-consuming, AFM also requires a flat substrate, which is not given at any time during the sample preparation process. On the other hand, in transmission optical microscopy, thin multilayer TMDCs with different thicknesses are easily distinguished. As shown in Figure 17, they exhibit different colors due to interference effects.

We thus aim at establishing a link between transmittance at different wavelengths and thickness of the sample. For this, the thicknesses of several WS_2 and WSe_2 samples on glass substrates are measured using an AFM. Additionally, optical microscope images in transmission are recorded. To quantify the transmitted intensity in different wavelength ranges, three different bandpass filters are used (ranges: 406-422 nm, 628-672 nm, 773-812 nm, filters from AHF Analysentechnik). With a monochromatic camera, we record images of the sample and the background. Then, the gray-scale value of the sample is divided by the gray-scale value of the background. This quantity is independent of the illumination intensity. For free-standing samples, it corresponds to the transmittance of the sample. In order for the method to be valid, several requirements have to be fulfilled:

- The illumination should be as homogeneous as possible. The two areas of the image (sample/background) should be as close to each other as possible.

- The gamma correction of the recorded image must be set to 1. Then, the grayscale value is proportional to the intensity (assuming constant camera sensitivity within the bandwidth of the filter).

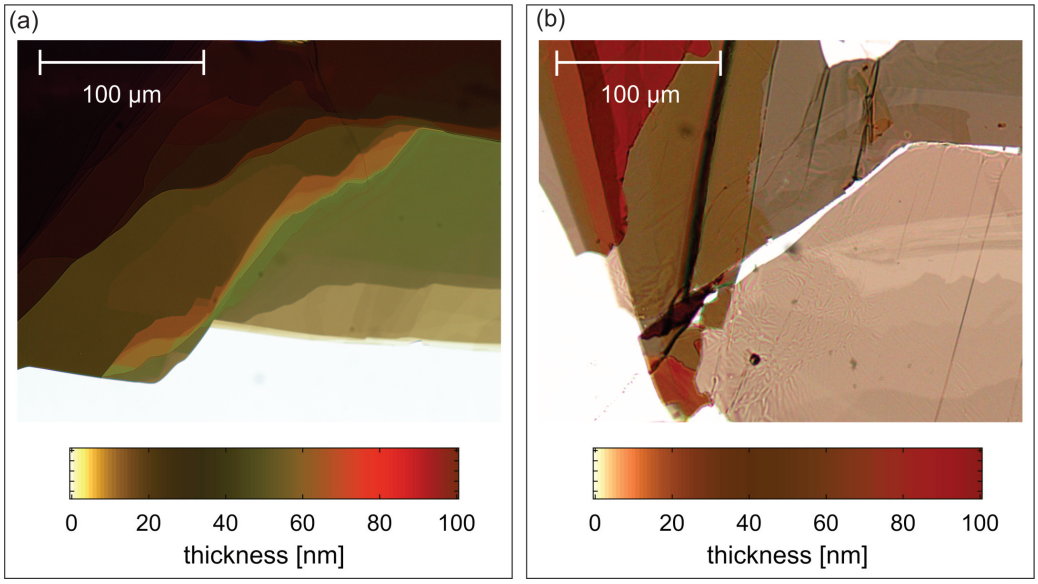

Figure 17: Optical microscope image of WS_2 (a) and WSe_2 (b) flakes recorded in transmission. Areas of different thickness can be distinguished by their color. Below the image, the approximate color-thickness relationship based on simulated transmission spectra is shown (see text for details on the simulation).

- Care must be taken not to saturate the background or parts of it. The images used for the calculations thus appear rather dark.
- The response of the camera must be linear. This is verified by taking images with different exposure times under the same illumination.
- Reflections of stray light on the surface of the flake should be minimized, for example by placing a narrow cylinder of blackout material around the flake.
- When comparing the measured values to literature values, it should be kept in mind that the spectrum of the white light source and the sensitivity of the camera influence the measured transmission. Relatively narrow bandpass filters should be used.

In order to verify the validity of the approach, the transmittances of neutral density filters with different optical densities were measured. The results are in Appendix A. In general, the measured values agree well with the expected ones. This confirms that the approach is valid for transmittance measurements. At the same time, this comparison provides a rough estimate for the accuracy of the method: For transmittances of 0.3 and more, the relative accuracy is around 10% while for lower transmissions a relative error of 20% has to be assumed.

In the next step, we measure the thickness of several WSe_2 and WS_2 flakes on glass substrates using an AFM. Then, we relate the thicknesses and the transmission measured by the method described above. Note that our method measures the transmittance only if the sample is free-standing. For samples on transparent substrates, the same calculation provides a quantity that cannot be directly related to the transmittance. This is due to the fact that the intensity transmitted through the substrate is not equal to the intensity transmitted at the substrate-sample interface, because the refractive indices of the sample and air are different. Consequently, the substrate has to be included in the analysis.

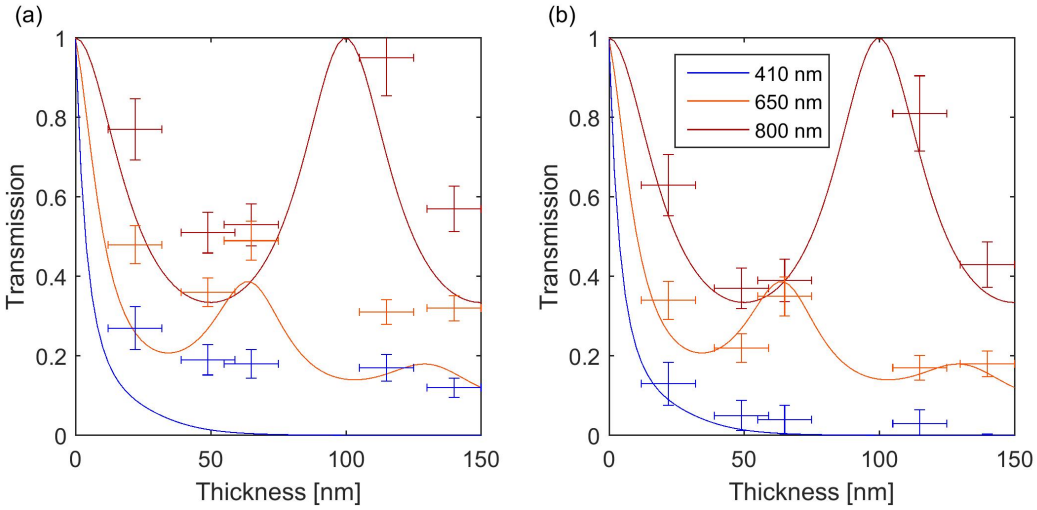

Figure 18: Panel (a) displays the results of the transmission measurements and simulated transmission over layer thickness for WS_2. In Panel (b), the experimental results are corrected by subtracting an empirical constant offset of $\Delta T = 0.14$. The glass substrate is taken into account in the simulations.

Since the samples are thin films with thicknesses in the range of tens of nanometers, interference effects play a role. In order to interpret the obtained transmission data and to relate it to the optical properties of the materials, it is thus necessary to perform calculations which take these effects into account. We use the program IMD [Win98], a software for calculating optical functions of multilayer structures from the optical constants (wavelength-dependent refractive index and extinction coefficient) of the constituent materials. We use literature values from [Bea76] and [Eic14] for the optical constants of WS_2 and WSe_2, respectively. We take into account the glass substrate and the fact that in our measurement the transmission is measured relative to the transmission of the substrate (see above). Figure 18 displays experimental thickness-transmission relationship together with the simulation results for WS_2. Note that the transmittance at 800 nm and 650 nm exhibit pronounced interference effects. This is due to the low absorption in this wavelength region, especially at 800 nm, where only indirect transitions can be excited in WS_2. The interference effects are almost absent at 410 nm, where due to the high photon energy many transitions can be excited and thus the penetration depth is short. The experimental data is able to qualitatively reproduce the shape of the curves, including interference effects. However, there is an offset of $\Delta T \approx 0.14$ between experimental values and simulation results. Furthermore, the behavior of the experimental transmission in the wavelength range of 406-422 nm, which decays quickly but then remains around 0.15-0.2 is not a physically reasonable result. Regardless of the exact values of the optical functions, the thickness-dependence of the transmittance of any thin film behaves like an exponential that is modulated by interference effects (whose magnitude depends on the penetration depth). Consequently, we assume a constant offset of $\Delta T = 0.14$ for the experimental values. This could be caused for example by scattered light that gets reflected on the surface of the flake. Figure 18 (b) displays the corrected values. They agree well with the results from the simulation.

Figure 19 displays the corrected experimental values and the simulation results for WSe_2. In the wavelength ranges of 773-812 nm and 628-672 nm, the corrected experimental values agree well with the simulation. For the wavelength range of 406-422 nm,

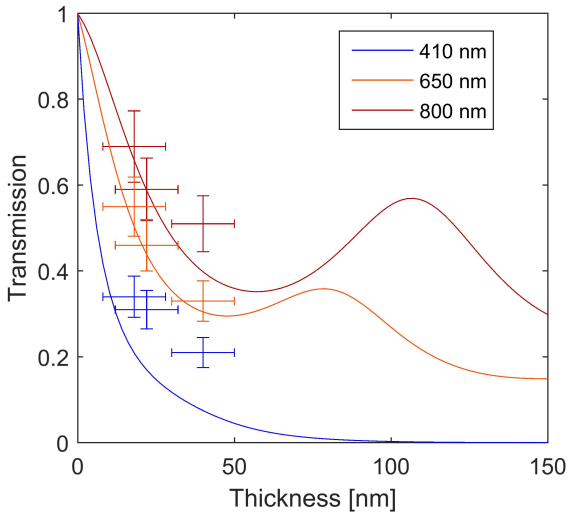

Figure 19: Comparison of the measured transmission-thickness relationship with the simulated transmission for WSe_2. The measured transmission values were corrected by $\Delta T = +0.14$ based on the results for WS_2, see Figure 18 and text for details.

experimental and simulation values differ.

In the following, we therefore use the filter in the wavelength range of 628-672 nm to estimate thicknesses. Then, we use the result together with the optical constants of the material to calculate its optical properties (for example its absorbance). Knowing the thickness and optical properties of the materials is an important prerequisite for the interpretation of time-resolved experiments: First of all, it is necessary to know, at least roughly, the initial distribution of hot carriers excited by the pump pulse. Secondly, the behavior of a heterostructure can depend on the thicknesses of the individual materials. For example, the total heat capacity of each material depends on its thickness.

5 Time-resolved diffraction results

5.1 Structural dynamics of the individual materials

Before interpreting time-resolved diffraction data of heterostructures, it is useful to know the structural dynamics of the individual materials. We thus perform measurements on free-standing WSe_2 and WS_2 samples. As an example, Figure 20 shows the diffraction image of freestanding WSe_2.

In all measurements, to obtain the Bragg peak intensities from the diffraction images, we sum over the number of counts within a circle around each Bragg peak. We analyze 60 Bragg peaks, from the (100) peak family to the (400) peak family. The time trace of the Bragg peak intensity is normalized to the equilibrium value at room temperature.

Figure 21 displays the time-resolved diffraction results for free-standing WSe_2 and WS_2. The thickness of the WSe_2 sample is (39 ± 10) nm and the thickness of the WS_2 sample is (32 ± 5) nm. The measurements are performed using a pump center wavelength of 400 nm. In both cases, the attenuation of the Bragg peak intensity can be described well by a single-exponential behavior. For both materials, we obtain the same time constant of (1.3 ± 0.2) ps (WS_2) and (1.3 ± 0.1) ps (WSe_2). The time constant reflects the efficiency of the energy transfer from the hot electrons to the lattice. Therefore, it is a measure of the strength of the electron-phonon coupling. For WSe_2, the result agrees well with previous measurements [Ber], which furthermore show that the time constant is independent of the pump laser fluence. Since WS_2 is a very similar material, we assume its time constant to be fluence-independent as well.

Panels (b) and (d) of Figure 21 display the dependence of the intensity attenuation on the scattering vector. It is described well by a linear behavior with a small positive y-axis intercept. This indicates that the samples are thin enough such that the kinematic scattering limit is fulfilled to a good approximation. If the kinematic scattering limit is fulfilled perfectly, that is in the absence of secondary scattering, the points should lie on a line that crosses the origin (compare Equation 13). In our case, a small contribution

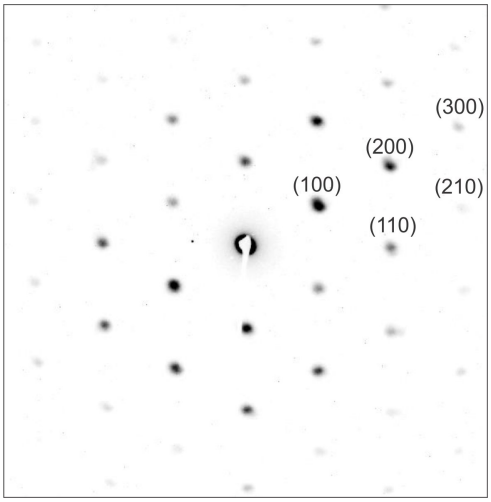

Figure 20: Diffraction image of free-standing WSe_2 with a thickness of 40 ± 10 nm at 60 keV electron energy. The hexagonal symmetry of the diffraction pattern reflects the in-plane symmetry of the crystal. The intensity of the Bragg peaks differs between diffraction spots belonging to the same peak family. This indicates a slight tilt of the sample with respect to the electron beam. The zero order beam is blocked.

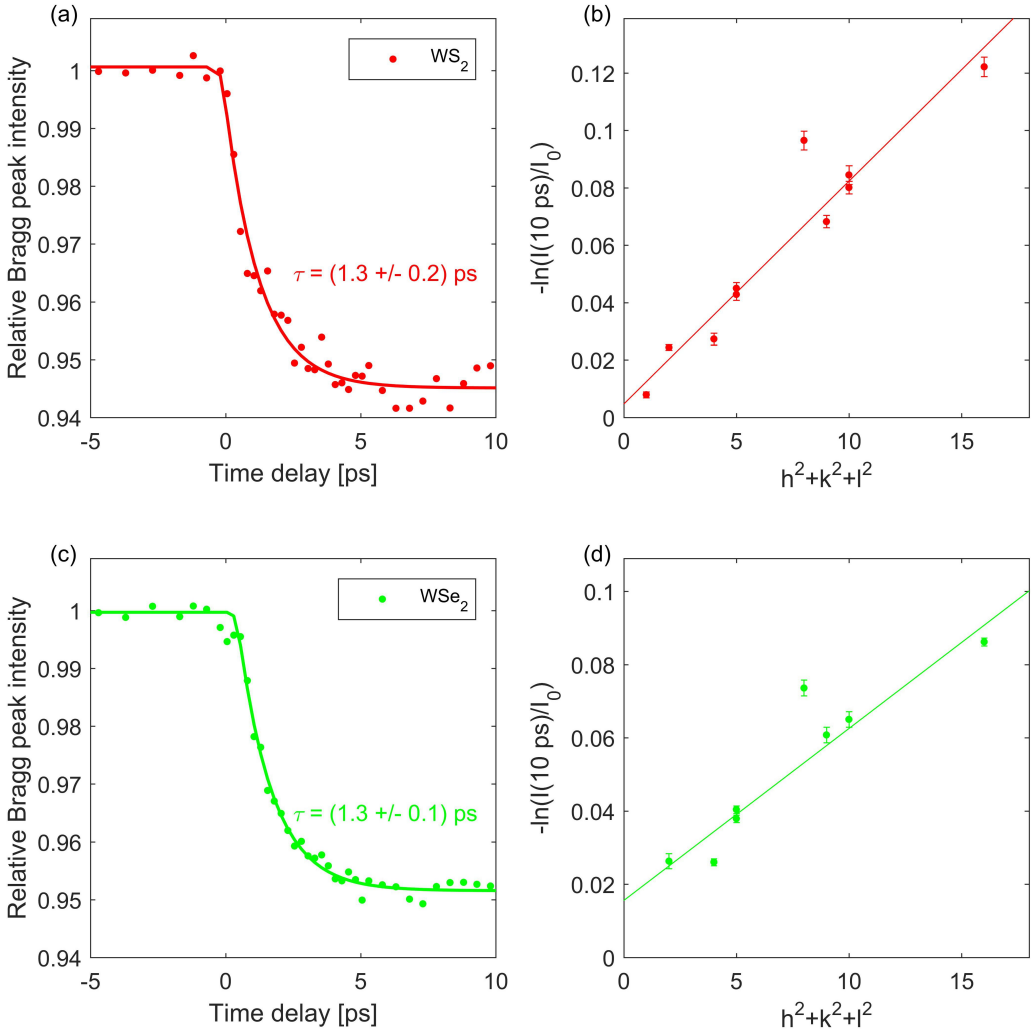

Figure 21: Time-resolved diffraction results for free-standing WS_2 and WSe_2. The photon wavelength used in these measurements was 400 nm. Plots (a) and (c) show the time trace of the Bragg peak intensity for a free-standing WS_2 and WSe_2 sample, respectively. Here, the median of all observed Bragg peaks is displayed. In plots (b) and (d), the logarithm of the relative intensity after the energy transfer to the lattice (here: after 10 ps) over the scattering vector is displayed.

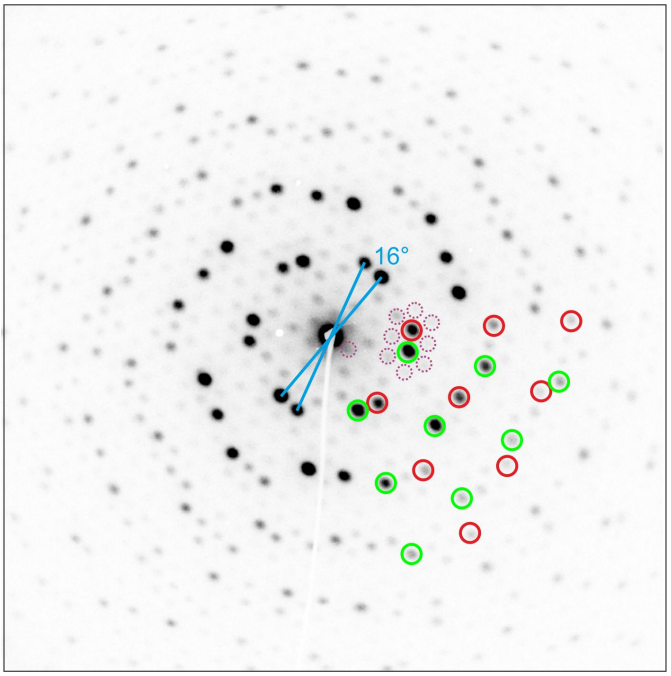

Figure 22: Diffraction pattern of a WS_2/WSe_2 heterostructure. The reciprocal lattices (and thus also the real-space lattices) are rotated relative to each other by an angle of 16°. The individual reciprocal lattices of the two materials (red: WS_2, green: WSe_2) as well as less intense extraordinary diffraction spots (dotted purple circles) can be identified. The diffraction image was recorded on sample number 1 (see Appendix B for sample details). For all the diffraction images recorded in this work we use an electron energy of 60 keV.

from secondary scattering exists. Interestingly, the y axis intercept and thus the amount of secondary scattering is bigger for WSe_2 even though the thicknesses of WSe_2 and WS_2 are comparable. This is due to the higher scattering form factor of selenium compared to sulfur (see Figure 10). Contributions from secondary scattering lead to attenuation of the zero-order beam. This effect becomes important when analyzing time-resolved diffraction of heterostructures, and will be discussed in the next section.

5.2 Structural dynamics of the WS_2/WSe_2 heterostructure

5.2.1 The diffraction pattern

The diffraction pattern of a WS_2/WSe_2 heterostructure is shown in Figure 22. The two superimposed reciprocal lattices of the individual materials can be identified (red and green circles). They are rotated relative to each other by an angle of about 16°, which means that in real space, the crystals of the two materials are rotated by the same angle.

Due to the hexagonal symmetry of the WSe_2 layers, for each material there are six Bragg peaks with the same magnitude of the scattering vector. In the following, these are called a 'peak family'.

Intensity differences between peaks of the same peak family can be observed. This indicates that the incidence of the electron beam is not perfectly normal, but deviates by a small angle due to a slight tilt of the sample. In addition to the main Bragg peaks, diffraction spots with much weaker intensity are also observed, which are due to diffraction beyond the kinematic approximation (compare Section 3.2.4).

5.2.2 The treatment of zero-order effects (ZOE)

As described in Section 3.3, in cases where the sample is thick enough such that a significant amount of secondary scattering occurs, the (000) spot of the diffraction pattern is also attenuated when the phonon population rises. Since electrons interact strongly with matter, this is often the case even for relatively thin samples. The samples used in our experiment are multilayer samples with thicknesses of several tens of nanometers. Furthermore, they contain rather heavy elements that scatter strongly, which is why the effect is non-negligible. In the case of a sample consisting of just one material, the zero-order effect (ZOE) alters the dependence of the attenuation on the scattering vector. Hence, if not accounted for, the ZOE leads to a systematic error in the determination of the sample temperature. The time behavior of the dynamics remains unchanged compared to the kinematic limit. For heterostructures, ZOE are more problematic because a ZOE in one material leads to the attenuation of all diffraction peaks of the other material. This means that the dynamics of one material gets imprinted on the time traces of the peaks originating from the other material. Figure 23 illustrates the effects of zero-order attenuation on the time traces for two fictitious examples. The entanglement of the time traces poses a challenge to the separate observation of the dynamics and makes a very careful analysis of the time traces necessary. The key to disentangle the dynamics of the two materials is the dependence on the scattering vector: ZOE lead to Bragg peak attenuation of the other material that is independent on the scattering vector. In contrast, a temperature rise in the material always leads to a scattering vector dependent attenuation[6] (compare Equation 22 of Section 3.3). Equation 22 suggests that in the case of a heterostructure, the s^2-dependence of the materials is linear with a non-zero y-axis intercept, which is the same for both materials[7]. Consequently, we analyse the time traces of heterostructures as follows: we fit the scattering vector dependence of the two materials with two linear curves. In the fit, we impose the constraint that both lines have the same y-axis intercept. Only if a material exhibits a non-zero slope under this constraint, we can interpret this as a rise of the phonon population in the respective material.

Apart from causing misleading time traces, zero-order effect may also lead to systematic errors in the determination of time constants. To better understand these systematic errors, we performed single-exponential fits on model data. Since the carrier-lattice energy transfer in WS_2 and WSe_2 can be well described by a single-exponential function (compare with results of Section 5.1), we assume a single-exponential behavior:

$$I(t) = 1 - c_1 \left(1 - \exp\{-\frac{t}{\tau_1}\}\right) \tag{23}$$

To model the zero-order effect (ZOE), we use another single-exponential function with a magnitude $c_2 < c_1$ and a different time constant τ_2:

$$I_{\mathrm{ZOE}}(t) = 1 - c_2 \left(1 - \exp\{-\frac{t}{\tau_2}\}\right) \tag{24}$$

The resulting time trace $I_{\mathrm{total}}(t) = I(t) \cdot I_{\mathrm{ZOE}}(t)$ is fitted with a single-exponential function. The resulting value is compared to the real time constant τ_1. Figure 24 displays the deviations from τ_1. In general, ZOE slower than the real time constant perturb the result

[6] Except in the limiting case of a very thick crystal, where the attenuation is equal for all diffraction orders. This is not the case for our samples.

[7] More precisely, the y-axis intercept of the heterostructure is the sum of the y-axis intercepts that would be measured on the materials if they were free-standing.

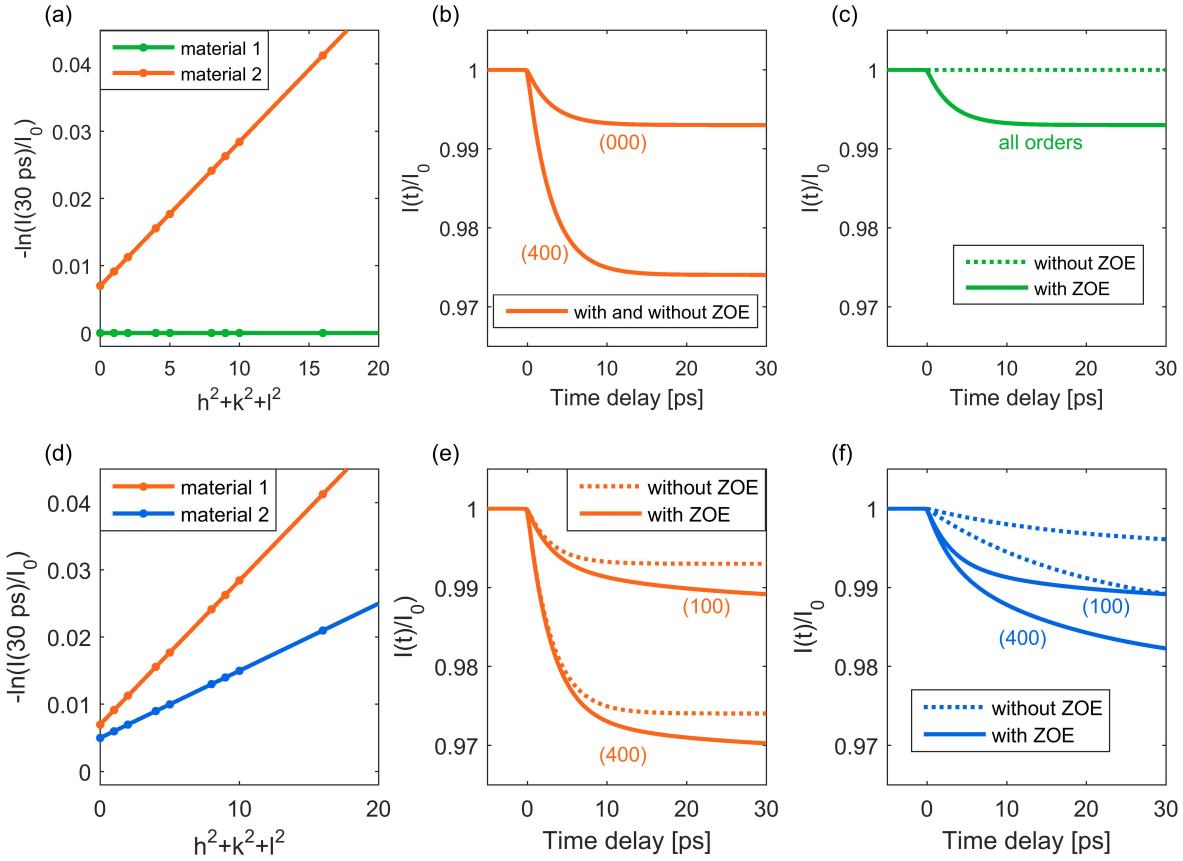

Figure 23: Explanation of the influence of zero-order effects (ZOE) on the time traces of two materials forming a heterostructure. Two different fictitious examples are shown. Panels (a)-(c) illustrate the case when only material 1 shows a response to photoexcitation. Panel (a) shows the s^2-dependence of the attenuation in the absence of ZOE. The intercept with the y axis determines the magnitude of the ZOE on the other material, respectively. In Panel (b), the time trace of material 1 is shown, which is not affected by ZOE. A single-exponential decay is assumed. Panel (c) shows the time trace of material 2. Even though the material shows no response to photoexcitation, the intensity of its Bragg peaks is attenuated due to ZOE. The attenuation is independent on the scattering vector. Panels (d)-(f) illustrate the case where both materials show a response to photoexcitation, but with different time constants. The phonon population of material 1 rises with a time constant of 3 ps while material 2 exhibits a much slower dynamics with a time constant of 20 ps (a single-exponential behavior is assumed for both). A similar situation could arise if only material 1 is photoexcited and equilibrates with material 2 via phonon-phonon coupling. Here, both materials are thick enough such that ZOE are non-negligible, as can be seen from the non-zero y axis intercepts in Panel (d). In Panels (e) and (f), the time traces in the presence of ZOE (solid lines) are compared to the time traces without ZOE (dashed lines). Both materials are affected by ZOE, which can lead to a systematic error in the determination of the time constants. In general, higher order peaks are less affected by ZOE than lower order peaks.

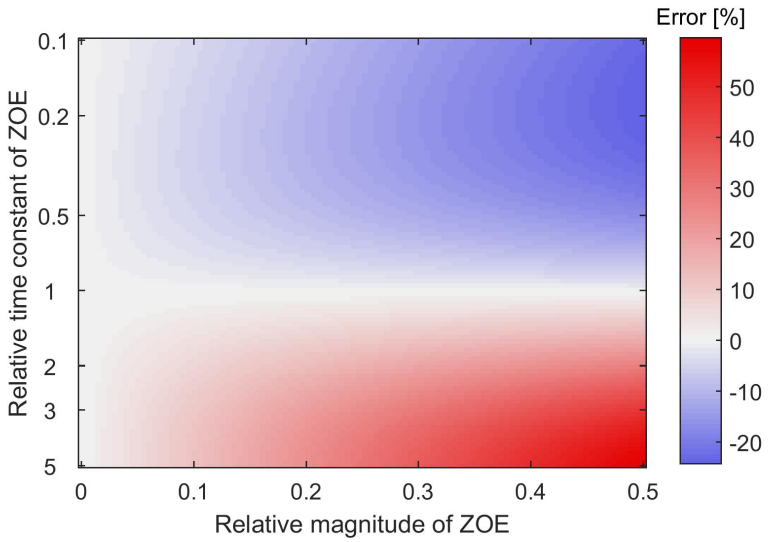

Figure 24: Simulation of the relative error of time constants due to ZOE. The x-axis shows the magnitude of the ZOE relative to the magnitude of the signal. The y-axis corresponds to the time constant of the zero-order effect relative to the time constant of the signal. A single exponential behavior for both signal and ZOE is assumed.

significantly more than faster ZOE. Slower ZOE lead to too large time constants while fast ZOE lead to time constants that are too small. Furthermore, the more similar the two time constants are, the less pronounced the error introduced by ZOE is. In particular, based on this simulation, it is possible to estimate the maximum error of the measured time constants.

5.2.3 Structural dynamics of the WS_2/WSe_2 heterostructure induced by 400 nm excitation

We perform time-resolved measurements on WS_2/WSe_2 heterostructures using a photon energy of 3.1 eV (400 nm pump center wavelength). The sample is excited from the side of WSe_2 at nearly normal incidence. From the thicknesses of the flakes and their optical properties, we estimate that for all samples more than 75% of the total absorbed energy is absorbed in WSe_2 (see Appendix B for details). Consequently, most of the excited carriers are initially located in WSe_2. Note that this reasoning is valid only if the absorption is not altered significantly by the laser pulse. In general, strong photoexcitation can lead to bleaching of transitions, and thus to a change in the absorption of the sample. However, for 400 nm excitation, this effect is expected to be weak for two reasons: First of all, many transitions can be excited. Hence, the number of excited carriers at a specific point in k-space is low. Secondly, most carriers are excited high above the band edges. Electron thermalization quickly changes the distribution of carriers in the Brillouin zone. Consequently, the transient population change at the transition points is not high enough to significantly alter the absorption.

Figure 25 shows the response of the relative Bragg peak intensities to photoexcitation. Both materials exhibit a decrease of the Bragg peak intensity that happens on a time scale of few picoseconds. The Bragg peak attenuation depends on the scattering vector for both materials. Consequently, in both materials the attenuation is caused by energy transfer to the lattice and not only by ZOE.

Figure 26 displays the dependence of the attenuation on the scattering vector. The

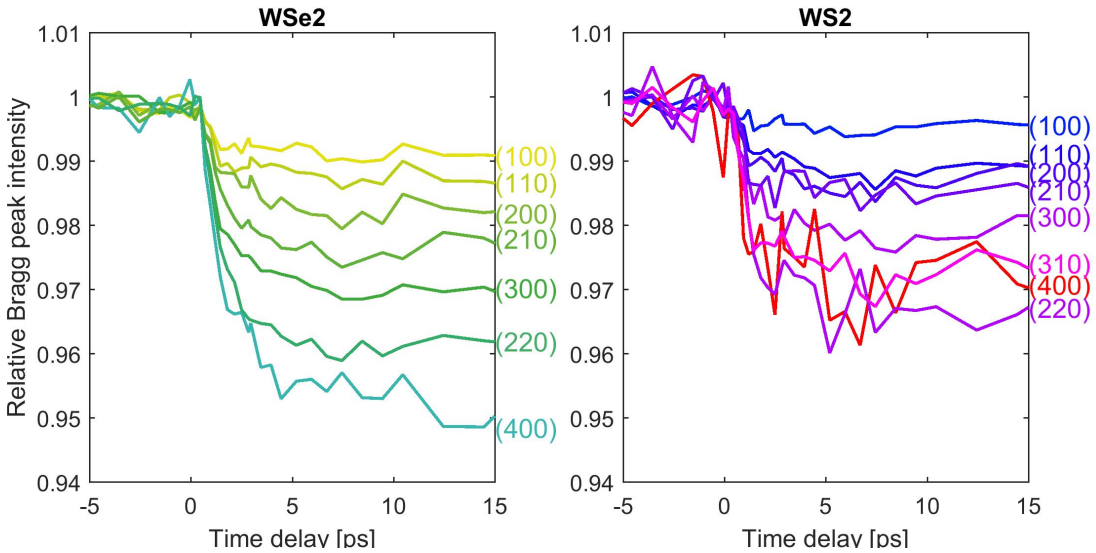

Figure 25: Relative Bragg peak intensity as a function of time delay for the Bragg peaks of WS_2 and WSe_2. Each curve corresponds to the mean of all peaks belonging to the respective peak family. The pump laser fluence in this measurement was around 0.6 $\frac{\text{mJ}}{\text{cm}^2}$.

values for $\frac{I(15\,\text{ps})}{I_0}$ were obtained by fitting each curve of Figure 25 with a single-exponential function. Based on the discussion of ZOE in heterostructures (Section 5.2.2), we fit the two curves of Figure 26 using two coupled linear regressions with the same y-axis intercept. The resulting values are $(8 \pm 2) \cdot 10^{-3}$ for the y-axis intercept, $(1.9 \pm 0.4) \cdot 10^{-3}$ for the slope of the curve for WS_2 and $(2.8 \pm 0.4) \cdot 10^{-3}$ for the slope of the curve for WSe_2. The difference in the two slopes expresses the observation that the relative change in Bragg peak intensity is lower for WS_2.

Figure 27 shows the experimental data for time delays up to 1 ns. After the initial decay, the Bragg peaks of the two materials evolve parallel to each other. Consequently, there is no further energy transfer between them. The slow recovery of the intensity corresponds to an overall cooling of the sample. From these results, we infer that the equilibration between the two materials is already finished at short time delays of 10 ps or less. The different magnitude of the Bragg peak attenuation stems from different Debye-Waller factors. Indeed, recalling the qualitative discussion in Section 3.3, we expect WSe_2 to have a larger Debye-Waller factor than WS_2 due to the lower frequencies of its phonon modes.

From the experiments presented in Section 5.1, we know the structural dynamics of free-standing WS_2 and WSe_2 after 400 nm excitation. The energy transfer from the hot electrons to the lattice can be described by a single exponential behavior with a time constant of around 1.3 ps. In the case of the WS_2/WSe_2 heterostructure where mostly WSe_2 is excited, one could expect a delayed structural response for WS_2: Most of the excited carriers have to transfer to WS_2 before creating phonons there. If the timescale for carrier transfer across the interface was equal or larger than the electron-phonon equilibration, this would lead to a slower attenuation of the Bragg peak intensity in WSe_2. However, in our experiment we observe dynamics that can be well described by a single-exponential behavior with the same time constant as for free-standing WS_2. We thus conclude both the transport within WSe_2 and the carrier transfer across the interface happens on a time scale that is much faster than the time scale for electron-lattice equilibration. This result is in agreement with previous results, which observed

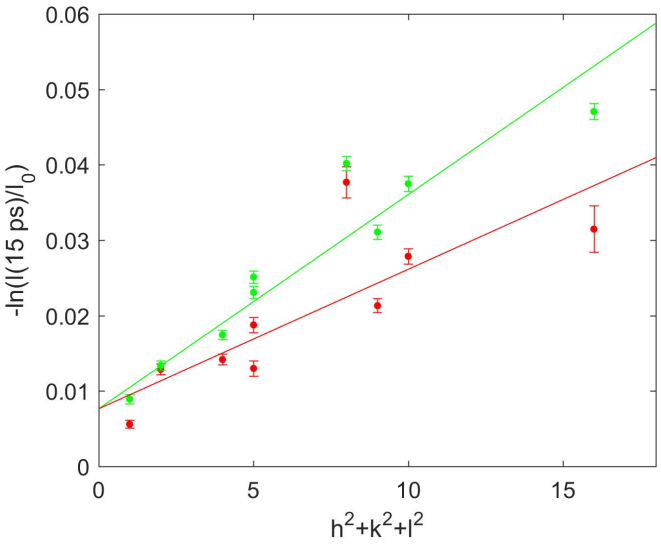

Figure 26: Natural logarithm of the relative intensity after 15 ps as a function of the squared scattering vector for the measurement of Figure 25. We obtain the data points from single-exponential fits of the time traces in Figure 25. The data is fitted with two linear regressions. We impose the constraint that both linear fits have the same y-axis intercept to account for ZOE (compare Section 5.2.2).

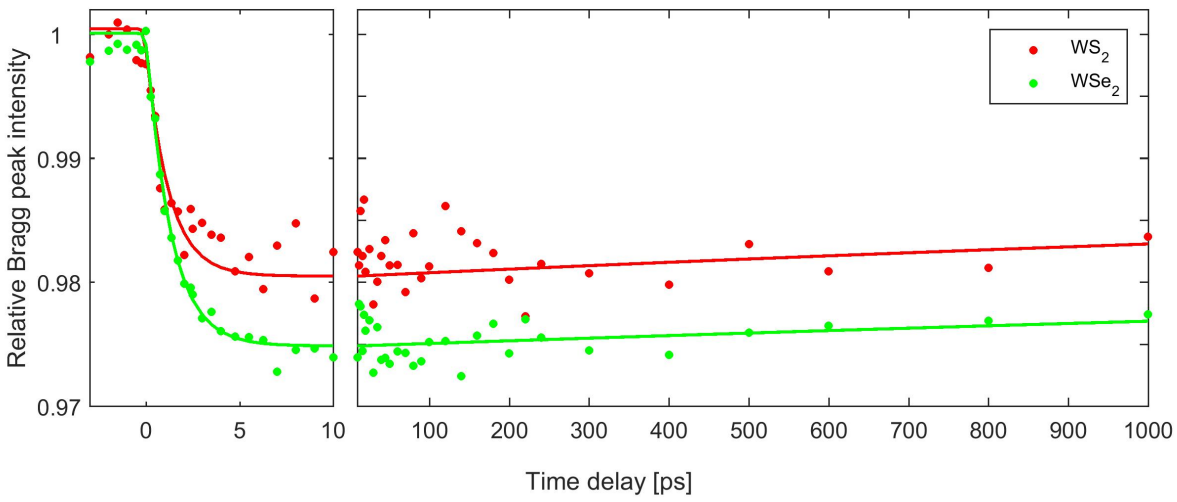

Figure 27: Behavior of the Bragg peaks of the two materials for time delays up to 1 ns. The median of all observed Bragg peaks is shown. No signs of equilibration processes between the materials at long time delays are observed. This measurement was taken at a pump laser fluence of around 0.6 $\frac{\mathrm{mJ}}{\mathrm{cm}^2}$.

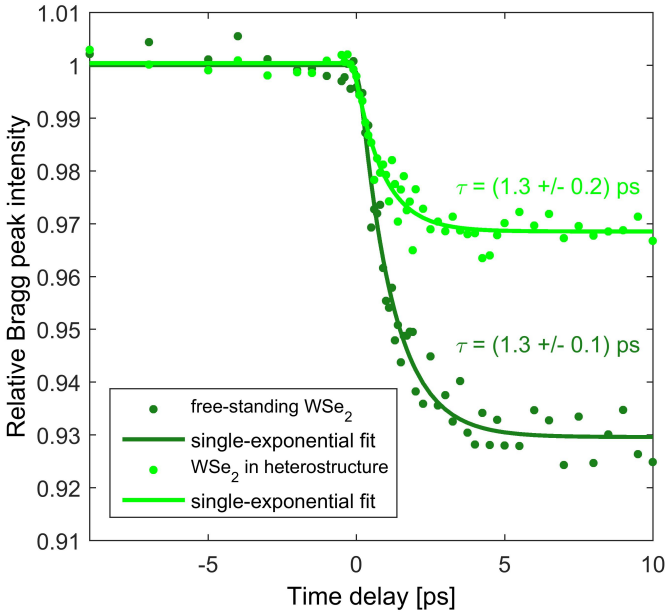

Figure 28: Comparison of the intensity attenuation for WSe_2 in the heterostructure and free-standing WSe_2 of the same thickness. The pump center wavelength is 400 nm and the same excitation fluence of 0.6 $\frac{\text{mJ}}{\text{cm}^2}$ is used in both measurements. In the case of WSe_2 as part of the heterostructure, the total energy transferred to the WSe_2 lattice is much smaller, indicating that a significant amount of energy is transferred to WS_2.

the charge transfer to occur within 100 ps or less [Hon14], [Che16].

In order to provide further evidence that energy is transferred between the two materials, we perform a reference measurement on free-standing WSe_2. For this, we use an area of sample number 1 where the WSe_2-flake is not covered by WS_2. The thickness of WSe_2 is the same as in the heterostructure, (40±10) nm. Furthermore, we use the same excitation conditions as for the experiment on the heterostructure. Due to the short penetration depth, it can be assumed that the amount of energy absorbed in WSe_2 is nearly equal despite the different interfaces for the outgoing pump beam (WSe_2/WS_2 and WSe_2/vacuum, respectively). Figure 28 shows the behavior of WSe_2 in both cases. The magnitude of the relative intensity decay is smaller for the heterostructure, indicating that a significant amount of energy was transferred from WSe_2 to WS_2.

From the single-exponential fits also shown in Figure 28, time constants of (1.3±0.1) ps for the free-standing WSe_2 and (1.3±0.2) ps for WSe_2 as part of the heterostructure are obtained. There is no difference in the efficiency of the energy transfer to the lattice.

The fact that the amplitude of the Debye-Waller-effect is smaller for WSe_2 as part of the heterostructure does not only indicate that energy is transferred across the interface, but also suggests that this happens before the electrons have relaxed to the conduction band minimum of WSe_2, that is on a time scale much faster than (1.3±0.1) ps. If the energy transfer was slower than the relaxation to the conduction band minimum of WSe_2, the electrons would deposit the same amount of energy in WSe_2 as in the case of free-standing WSe_2. After the transfer, additional energy, which is available due to the offset of the conduction band minima, would be deposited in WS_2. The fact that this is not observed provides further evidence for efficient carrier transfer across the interface.

So far, all the measurements were taken at a particular excitation fluence and thus at a particular density of excited carriers. In principle, the dynamics of the heterostructure

can depend on the excitation fluence, for example due to charging effects. Consequently, in the next step, we vary the excitation density by varying the pump laser fluence and investigate its effect on the structural dynamics. Figure 29 displays the result of the fluence-dependent measurements.

The slope of the curves in Panels (a) and (b) of Figure 29 relates to the total phonon population in the lattices. It is fluence-dependent for both materials. As expected based on Equation 22, the magnitude of ZOE (the y- axis intercept) also increases with increasing fluence. Figure 29 (c) shows the magnitude of the slope over the pump fluence. If bleaching effects are small, the pump fluence is proportional to the energy deposited in the sample. For samples with small ZOE, the slope of s^2-dependence corresponds to $B_k(T) - B_k(T_{\mathrm{ref}})$, where $B_k(T)$ is the Debye-Waller factor (compare Equation 13). The Debye-Waller factor in turn is proportional to the total mean squared displacement. Hence, it is proportional to the energy content of the lattice. Both curves of Figure 29 increase linearly with the pump fluence. The result indicates that the fraction of the total absorbed energy deposited in each material stays constant. Consequently, the fast equilibration between the materials is a fluence-independent effect. Figure 29 (d) shows that the time-constants for the energy transfer to the lattice are fluence-independent. This result confirms the observation of fast interfacial energy transfer for all fluences.

To summarize, the experiments on the WSe_2/WS_2 heterostructure after 400 nm photoexcitation show that a large portion of the hot carriers is transferred from WSe_2 to WS_2 within less than the time resolution of our setup (250 fs). The electronic coupling at these time scales already establishes equilibrium between the two materials. Furthermore, fast electronic coupling is observed independently of the excitation fluence.

In the 400 nm experiments, excited carriers have large initial excess energies. In general, the efficiency of the electronic transfer can depend on the excess energy. Therefore, in the next step, we examine the dynamics of the heterostructure after preparing excited electronic states with much less excess energy in WSe_2.

5.2.4 Structural dynamics of the WS_2/WSe_2 heterostructure induced by 800 nm excitation

In contrast to 400 nm, 800 nm excitation produces a very defined distribution of excited carriers, since carriers can only be excited at the K-point of WSe_2. Figure 30 displays the spectrum of the pump pulse and the absorption spectrum of WSe_2 and WS_2. Only a part of the pump pulse spectrum can excite WSe_2. The absorption of WS_2 is very small since only indirect transitions contribute. This excitation condition has two main differences compared to the 400 nm excitation: First, the location of the excited electrons and holes in WSe_2 in reciprocal space is known. Second, a rise in phonon population in WS_2 has to be caused by energy transfer across the interface, because WS_2 is almost not excited by the pump pulse.

Figure 31 displays the time-resolved diffraction results for an excitation fluence of about 10 $\frac{\mathrm{mJ}}{\mathrm{cm}^2}$ [8]. The s^2-dependence in Figure 31 (b) reveals that the phonon population rises in both materials. As in the previous measurements, the onset of the effect is the same for both materials. However, in contrast to 400 nm excitation, the time scale of the energy transfer is different: The time trace of WSe_2 exhibits a decay with a time

[8] This is a rather high fluence for time-resolved diffraction experiments. High fluences are necessary here for two reasons: First, the absorbance of WSe_2 in the wavelength region around 800 nm is low. Second, each carrier transfers relatively little energy to the lattice, so that much more excitation density is needed to obtain a reasonably high signal.

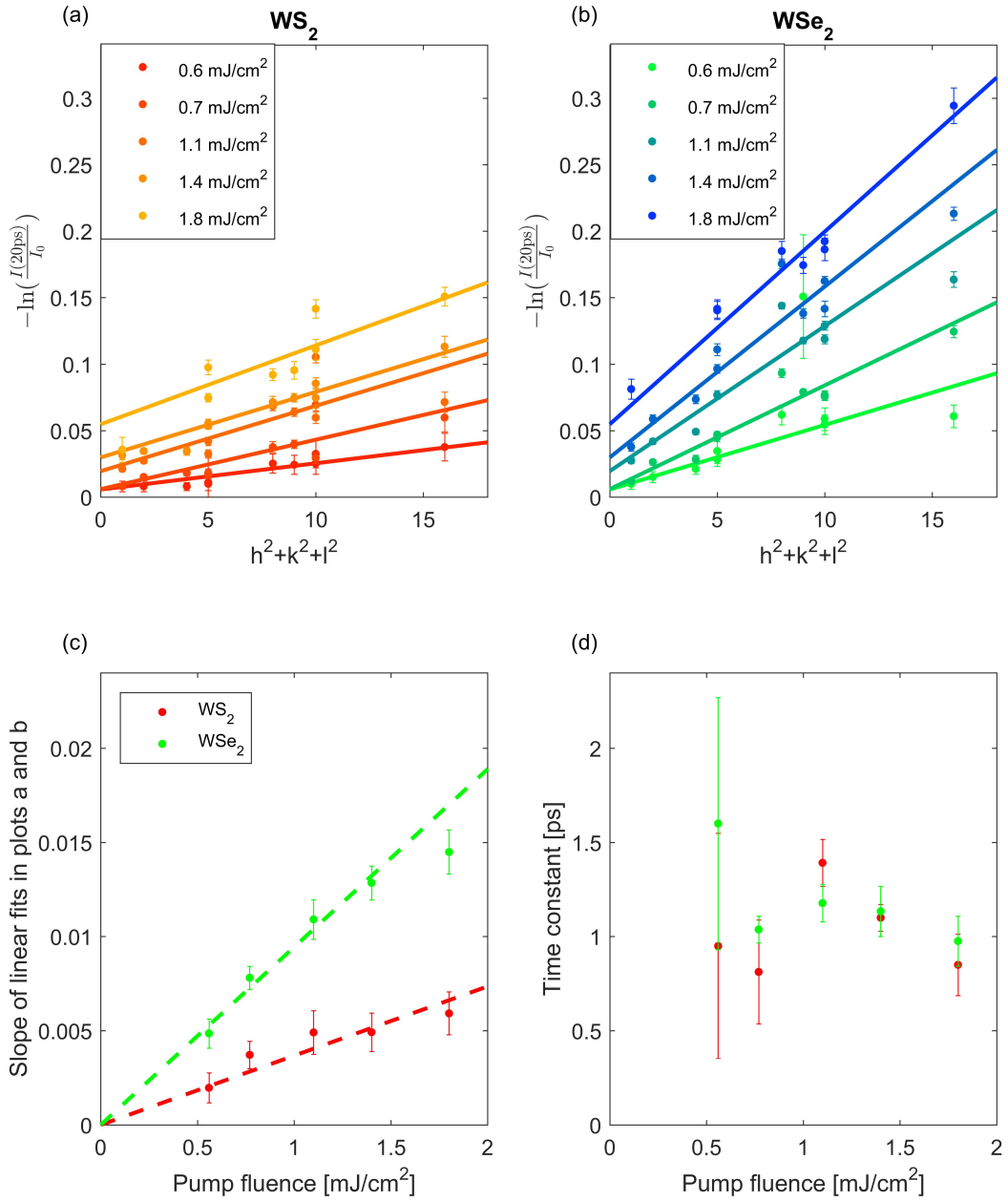

Figure 29: Fluence-dependence of the Bragg peak attenuation after 400 nm excitation. Panel (a) and (b) show the dependence of the Bragg peak attenuation on the squared scattering vector at different pump fluences for WS_2 and WSe_2, respectively. Panel (c) displays the slope of the linear regressions of Panel (a) and (b) over the pump fluence. Panel (d) displays the measured time constants over the pump fluence. The measurements were recorded on sample number 2 (see Appendix B for sample details).

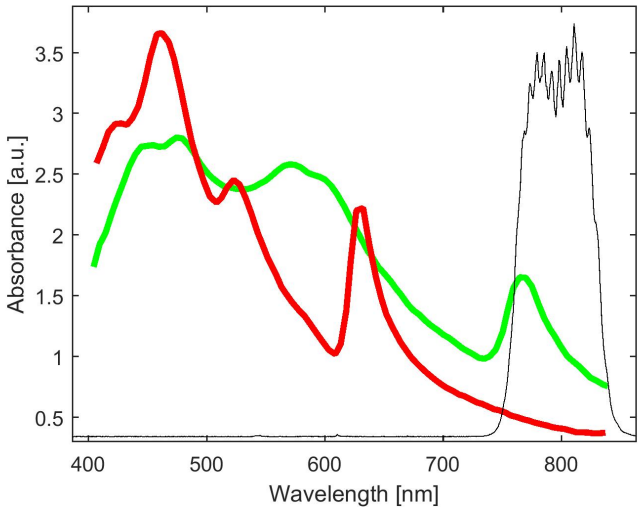

Figure 30: Absorption spectrum of bulk WSe_2 (green) and WS_2 (red), data from [Zha13]. The spectrum of the pump laser is shown in black. In WSe_2, the laser excites the first excitonic resonance (A exciton). In WS_2, only indirect transitions are excited. Consequently, excited charge carriers are created almost exclusively in WSe_2.

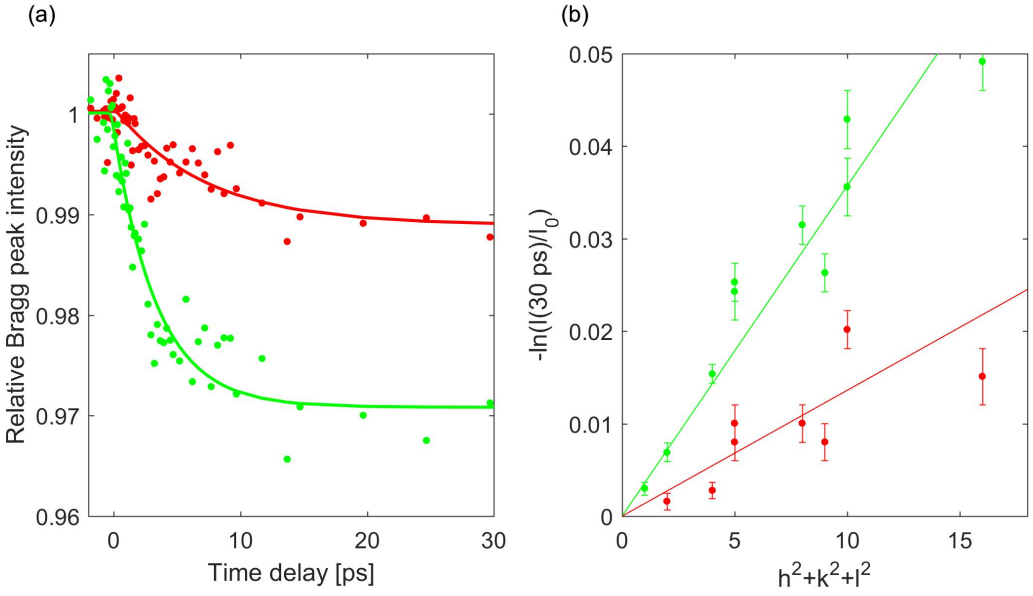

Figure 31: Structural dynamics of the heterostructure after 800 nm excitation. Panel (a) shows the time trace of the relative Bragg peak intensity. The median of all observed Bragg peaks is shown, except (100) and (110), which were excluded due to their high noise level. Panel (b) shows the dependence of the Bragg peak attenuation on the scattering vector. The excitation fluence of this measurement was about 10 $\frac{\text{mJ}}{\text{cm}^2}$. The measurement was performed on sample number 3 (see Appendix B for sample details).

constant of (3.4±0.5) ps. For WS_2, a significantly longer time constant of (7.2±0.7) ps is observed. The time constant of WSe_2 agrees well with previous measurements on free-standing WSe_2 [Wal17]. Compared to 400 nm excitation, the time constant is longer. This can be explained by the lower initial electronic temperature in the 800 nm measurements. In general, carriers with energies well above the conduction band minimum have more phase space available for electron-phonon scattering than carriers with energies close to the conduction band minimum. During the electron-lattice equilibration, each excited electron leads to the creation of multiple phonons[9]. In cases where the initial electronic temperature is high, the electron-phonon scattering rate is high in the beginning. As the electronic temperature decreases with time, the electron-phonon scattering rate becomes slower, because the available phase space becomes smaller. For this reason, faster time constants are observed for high initial electronic temperatures.

The time constant for the energy transfer to the lattice in WS_2 is expected to depend on the electronic temperature in a similar way. Nevertheless, the time constant observed for WS_2 is significantly longer than the time constant of WSe_2. This indicates that the transfer of hot carriers from WSe_2 to WS_2 is relatively slow: Electron transfer times which are slower than the electron-lattice equilibration in WS_2 lead to structural dynamics dominated by the slower 'bottleneck' process.

A possible explanation for the slow carrier transfer in the case of 800 nm is the existence of an energy barrier at the interface. Such an energy barrier can develop transiently due to charge separation. It particularly affects carriers excited with 800 nm due to their low temperature. The effect will be discussed further in Section 7.2.

In conclusion, the 800 nm experiments on the WS_2/WSe_2 heterostructure show that energy is transferred to both materials with a time constant of (3.4±0.5) ps (WSe_2) and (7.2±0.7) ps (WS_2). In contrast to the 400 nm experiments, the time scales differ for the two materials: WS_2 exhibits a significantly longer time constant. This indicates that the time constant for charge transfer across the interface is similar compared to the time constant for electron-lattice-equilibration.

[9]For pumping with 400 nm, carriers have large excess energies due to the excitation well above the conduction band minimum. In the 800 nm experiments, electrons have average excess energies of about 300 meV because of the indirect band gap of bulk WSe_2: Excited electrons are created at the K point but then relax to the bottom of the Σ valley.

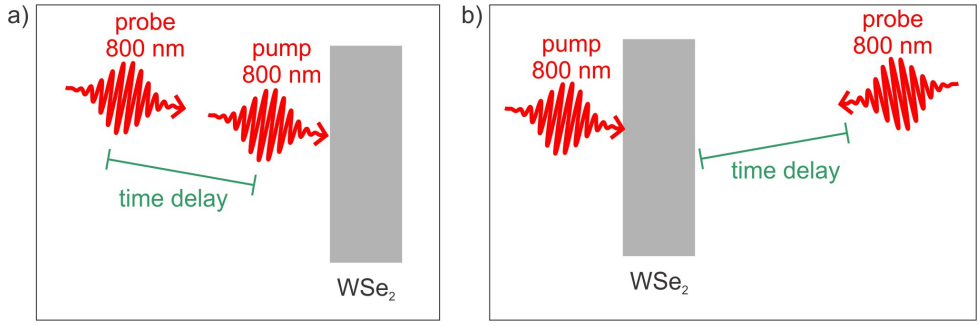

Figure 32: Scheme of the optical pump-probe experiments performed on WSe_2. Panel (a) illustrates front pump - front probe experiments. Here, pump-induced changes in the electronic and structural properties can be measured. Panel (b) shows the principle of front pump - back probe experiments. In this case, the signal also depends on the transport of hot carriers in the sample.

6 Time-resolved optical experiments on WSe_2

The time resolved diffraction experiments with 400 nm pump wavelength suggest an efficient charge transfer across the interface. Furthermore, in the 400 nm experiments, the penetration depth is short and thus most free carriers are created close to the interface vacuum-WSe_2. Consequently, the results suggest an efficient charge transfer also within WSe_2. To corroborate the latter result, we perform optical measurements on thick WSe_2. We compare two cases: In the first experiment, pump and probe beam are illuminate the same side of the sample (front pump - front probe). In the second experiment, pump and probe beam illuminate the sample on different sides (front pump - back probe). This is depicted in Figure 32. By comparing the results of the two measurements, conclusions about the transport of excited carriers in the sample can be drawn [Bro62]. We use a WSe_2 flake on fused silica, which is prepared by the method described in Section 4.2. The sample is displayed in Figure 33. Areas of different thicknesses can be distinguished. Measurements were performed on two areas with different thicknesses. Area 1 has a thickness of 750-900 nm and area 2 has a thickness of (130±20) nm (both measured by AFM).

Especially for the front pump - back probe measurements, a thin reference material with a fast response on the back side is needed in order to determine the delay at which

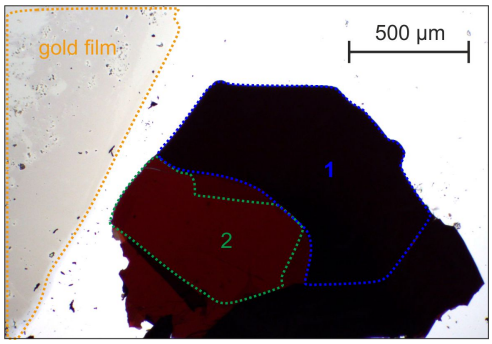

Figure 33: Optical microscope image of the WSe_2 sample used for the optical pump-probe measurements. Two different areas of the sample were examined, which are marked in the image. Area 1 is about 750-900 nm thick while area 2 has a thickness of only (130±20) nm (measured by AFM). The substrate is fused silica. On the side, a thin gold film was evaporated, which is used for determination of time zero in the time-resolved optical measurements.

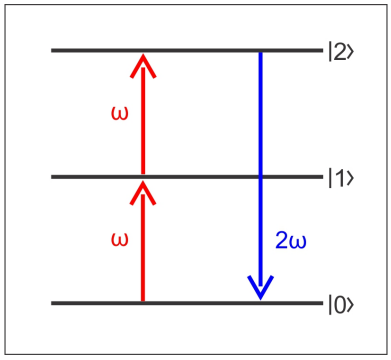

Figure 34: Schematic illustration of resonant second harmonic generation. A carrier is excited from the ground state to an intermediate state $|1\rangle$ and then to state $|2\rangle$. During this process, two photons are absorbed. When the excited carrier relaxes, it can emit a photon with double the incident frequency.

the pump pulse and probe pulse arrive simultaneously (time zero). For this, a thin gold film with a thickness of ca. 5 nm is evaporated close to the WSe_2 flake. For both the pump and the probe pulses we use a center wavelength of 800 nm.

In time-resolved optical experiments, several quantities can be measured, e.g. reflectance, transmittance, second harmonic generation (SHG) or ellipticity. In our experiments we record the reflectivity the SHG signal. Changes in reflectivity after photoexcitation reflect the changes in the population of the electronic bands. Some transitions are bleached while others become available. In the case of 800 nm excitation, only transitions at the K point can be excited. Consequently, the reflectivity signal probes the change in population only in this region of the Brillouin zone[10].

The SHG signal also measures changes in the electron population, albeit in a different way. The process of (resonant) second harmonic generation in a crystal involves three states which are separated by the same energy $\hbar\omega$: a populated ground state and two unpopulated excited states. Figure 34 illustrates the process. Changes in the SHG signal indicate population changes of states that are involved in the SHG process.

For inversion-symmetric materials, SHG is forbidden in the bulk. This makes SHG a surface-sensitive technique for many materials. WSe_2 is an inversion-symmetric crystal. However, the inversion symmetry stems from the 2H-stacking of the crystal - the individual layers are not inversion-symmetric. For few-layer samples, this leads to a strong variation of the SHG intensity between even/odd numbers of layers [Zen13], [Li13]. For thick samples, the incident pulse is attenuated significantly inside the sample. This can lead to a net SHG signal from the bulk, because the SHG contributions from the individual layers don't cancel perfectly. Consequently, it cannot be assumed that the SHG signal comes only from the surface, even though WSe_2 is inversion-symmetric.

To summarize, both changes in the reflectivity and the SHG signal indicate a change in the carrier distribution in the probed region. This change can be due to direct excitation or to transport processes. In both cases, relating the details of the signal to the underlying processes requires theoretical calculations of the excitation process and of the evolution of the system after excitation. Nevertheless, the onset of the hot-carrier-induced changes can be determined directly from the time traces.

Figure 35 displays the time traces of the reflectivity and SHG signal for both front and

[10]For electrons that have already been excited into the conduction band, more transitions are available. However, for moderate excitation densities, their contribution to the change in reflectivity is small.

back pumping. Note that the amplitudes of the signals vary slightly for different spots on the sample, but the general shape is reproducible. The time resolution of the setup is around 20 fs.

Comparing front and back pump experiments for the thin area, no significant delay is observed in the response to photoexcitation. However, the shape of the signal is different for back probing, indication of a different electronic distribution. For the thick area, the initial rise/drop of the signal is shifted both for reflectivity and SHG. The shift is 30 fs for the reflectivity signal and 20 fs for the SGH signal, which is already close/equal to the time resolution of the setup (20 fs).

To draw conclusions on the velocity of hot carrier transport in the material, it is necessary to take into account the finite penetration depth of the pulses, which is rather high at 800 nm. For this, we use the optical properties of WSe_2 (compare Section 4.3) to estimate the excitation profile of the pump pulse from its spectrum. Figure 36 (a) shows the spectrum of the pump pulse. Figure 36 (b) displays the resulting distribution of excited carriers. Since the different wavelength components of the pump pulse have different penetration depths, the total excitation profile is the sum of exponentials with different decay lengths. In particular, the wavelength components at the excitonic resonance decay quickly. The components with longer wavelengths have very large penetration depths. By comparing these results with the thickness of the two sample regions, we find that in the thin area, carriers are basically excited everywhere in the sample. Consequently, identifying the contributions of carrier transport is not possible in this case. However, the thicker area is thick enough such that few carriers are excited at the back side of the sample. To estimate the velocity of carrier transport, we calculate the average initial position of an excited carrier (dashed black line in Figure 36 (b)). The result is about 270 nm. Considering that the probe pulse penetrates the material by roughly the same amount, we estimate that the transport velocity of the excited carriers is on the order of 10 $\frac{\text{nm}}{\text{fs}}$. Note that this is a rough estimation due to the simplifications regarding the initial position of the excited carriers. Furthermore, the calculation of the excitation profile relies on the precise knowledge of the optical constants of WSe_2. Literature values for these don't always agree, especially in the relevant wavelength region around the A excitonic resonance (compare for example references [Eic14], [Bea76] and [Dav72]). Measurements on much thicker samples could yield more precise results for the transport velocity. Alternatively, a center wavelength of 400 nm could be used. In this case, the penetration depth is much shorter for all wavelength components.

In any case, the results of the optical measurements confirm the result of the time-resolved diffraction experiments with 400 nm pump center wavelength. The charge carrier transport in WSe_2 is fast on the time scales of the diffraction experiment: For the typical sizes of WSe_2, around 20-40 nm, and a transport velocity on the order of 10 $\frac{\text{nm}}{\text{fs}}$, all of the excited carriers can reach the interface in a couple of femtoseconds.

As mentioned in Section 3.3, excitation of WSe_2 with femtosecond laser pulses can also lead to the creation of coherent phonons. These can be observed as oscillatory changes of the signal in optical pump-probe experiments. Figure 37 shows the time traces of the differential reflectivity for delays up to 2 ps. Indeed, an oscillation is observed both for front and for back probing. Figure 38 shows the Fourier transform of the oscillatory part of the signal. The amplitude of the oscillation is (7.7±0.7) THz. WSe_2 has two phonon modes in this frequency region that are Raman-active and thus can in principle be excited: The E_{2g} phonon at 7.43 THz and the A_{1g} phonon at 7.54 THz [Ter14]. In our experiments the resolution is not sufficient to resolve the two frequencies. Hence, the

measured oscillation can correspond to either of the two modes or to a combination.

Comparing the amplitudes of the oscillation, it is reduced for back probing compared to front probing. This reflects the fact that in order to excite a coherent phonon, the electronic population needs to change very suddenly, within less than the period of the coherent phonon. The electronic excitation typically changes the charge distribution. This corresponds to a change of the potential energy landscape for the ions, which in response start to oscillate. On the front side, the short pump laser pulse causes the excitation of many electrons within a short period of time. Therefore, the requirement of a sudden electronic population change is fulfilled. In contrast, most of the electrons on the back side of the sample are not initially created there. They are transported from the front side to the back. The transport leads to an effective broadening of the excited electron pulse, which is reflected in the decrease of the amplitude of the coherent phonon.

An additional effect can contribute to the weakening of the coherent phonon: the populated excited states are different at the front compared to the back side. Initially, the excited carrier population is created at the K-point, but it quickly scatters to the Σ-valley for bulk WSe_2. Therefore, the transported electrons are likely to be in a Σ-state. Since not all of the excited electronic states have the right charge distribution to excite these particular coherent phonon(s), this effect may also contribute to the weakening of the oscillation.

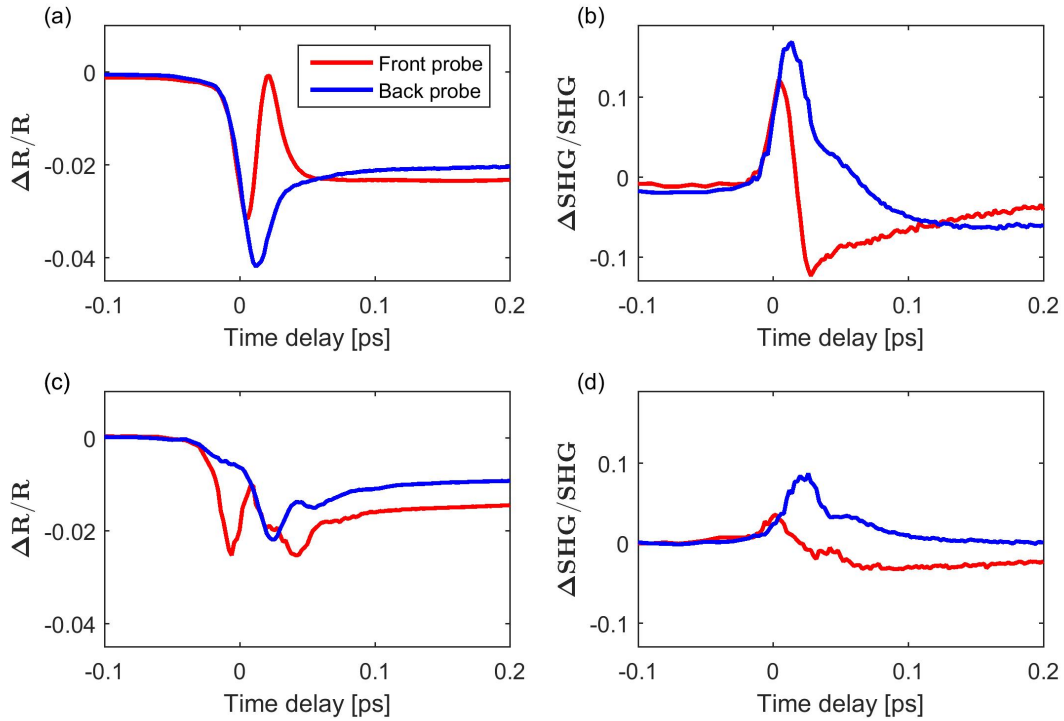

Figure 35: Time-resolved reflectivity and SHG measurements of WSe_2 photoexcited with 800 nm, comparison of front and back probing. The curves displayed in Panel (a) and (b) were measured on the thin area (thickness 130±20 nm). The data of plots (c) and (d) was measured on the thick area (thickness 750-900 nm).

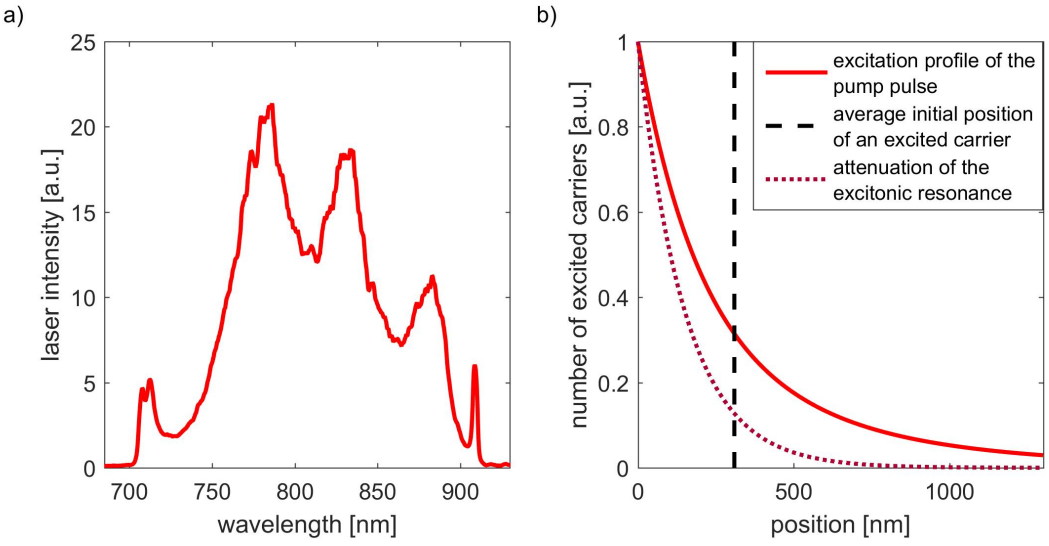

Figure 36: Laser spectrum and corresponding excitation profile in WSe_2. Panel (a) displays the spectrum of the pulses used in the time-resolved optical experiments. Panel (b) shows the number of excited carriers as a function of the distance from the sample surface (solid red line). For comparison, the penetration profile at the peak of the excitonic resonance is shown as well (dotted red line). The dashed black line indicates the average distance of an excited carrier from the surface. The calculations are based on optical constants for bulk WSe_2 by reference [Eic14].

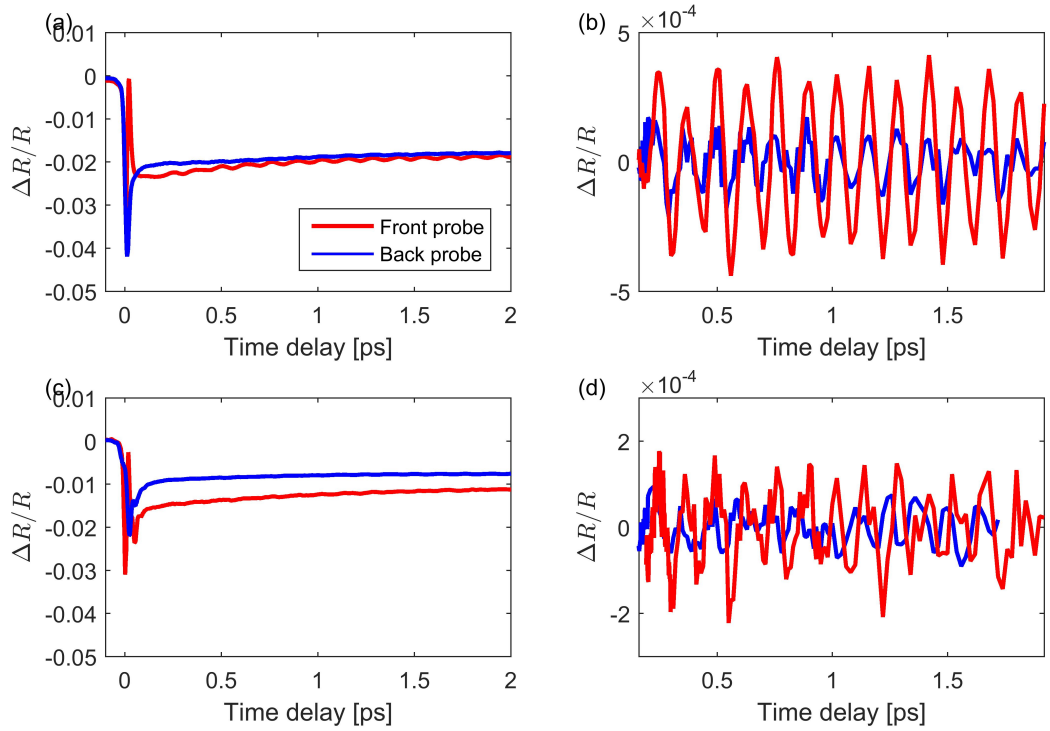

Figure 37: Differential reflectivity signal of WSe_2 for time delays up to 2 ps. The data of Panel (a) was measured on the thin area of the sample (thickness (130±20) nm), the data of Panel (c) on the thick area (thickness around 750-900 nm). The superimposed oscillation is due to the coherent phonon(s) excited by the pump laser pulse. Panels (b) and (d) display only the oscillatory parts of the signal for the thin and the thick area, respectively. In both cases, the amplitude of the oscillation is reduced for back probing.

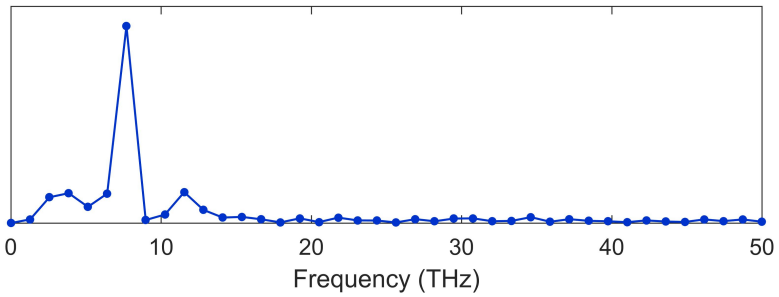

Figure 38: Fourier transform of the oscillatory part of the differential reflectivity signal. The peak corresponds to a frequency of (7.7±0.7) THz.

7 Discussion

7.1 Influence of the excitation energy on the heterostructure dynamics

We perform experiments using two different excitation energies, 1.6 eV (800 nm) and 3.1 eV (400 nm). Figure 39 (a) and (c) illustrates the initial distribution of excited carriers in each case.

The 800 nm excitation creates excited carriers almost only in WSe_2. Since the photon energy corresponds to the A-exciton resonance, all of the excited carriers are located close to the band edges. Since the penetration depth of the pump pulse is much larger than the thickness of WSe_2, the density of excited carriers is nearly constant in WSe_2. Figure 40 shows the excitation profiles of the pump pulses with 800 nm and 400 nm center wavelength.

Figure 39 (b) illustrates that after excitation, electrons can transfer to WSe_2. In contrast, the holes are confined to WSe_2 due to the band alignment. Experimentally, we observe a structural response in both materials. The signal in WS_2 indicates that carriers are transferred across the interface after excitation. This is in agreement with the expected behavior.

In contrast, 400 nm excitation produces a very different initial hot carrier distribution. Many transitions can be excited at this photon energy. Hot electrons (holes) can be found well above the conduction band minimum (well below the valence band maximum). In this case, the density of excited carriers in WSe_2 is not homogeneous: most of the excited carriers are created close to the surface of WSe_2. Since the photon energy is well above the band gap energy of WS_2 as well, some carriers are excited in WS_2. Figure 39 (d) illustrates the initial hot carrier distribution. All of the electrons as well as many holes are able to cross the interface. Transfer and carrier-carrier-scattering is expected to lead to a carrier distribution with more electrons in WS_2 and more holes in WSe_2. Hence, a charge imbalance develops. This is illustrated in Figure 39 (f).

In the 400 nm experiment, a structural response is observed in both materials as well. The reference measurements on free-standing WSe_2 indicate significant charge transfer across the interface, which agrees well with what is expected from the band alignment.

While for both excitation conditions a significant amount of charge is transferred across the interface, the dynamics of the rise in lattice energy of WS_2 is different in each case: For 400 nm excitation wavelength, the time constant for the Bragg peak attenuation of the WS_2 peaks is the same regardless whether the materials are part of a heterostructure or not (1.3 ps). Since most of the excited carriers are produced in WSe_2, this means that the carrier transfer has to be much faster than 1.3 ps. Otherwise, the transfer process would delay the rise of lattice energy in WS_2. In contrast, for 800 nm excitation wavelength, the rise time of the signal in WS_2 is large: (7.2 ± 0.7) ps. This is significantly larger than the time constant for the energy transfer to the lattice of WSe_2, (3.4 ± 0.5) ps. A comparison of WS_2 as part of the heterostructure and free-standing WS_2 is not possible, because it cannot be excited at 800 nm. However, due to the similarities of the two materials, it is valid to assume that the time constant of free-standing WS_2 should have a value close to the time constant of WSe_2. The large time constant of WS_2 in our experiment suggests that for this particular excitation condition, the interfacial carrier transfer is slow enough to delay the rise of lattice energy in WS_2.

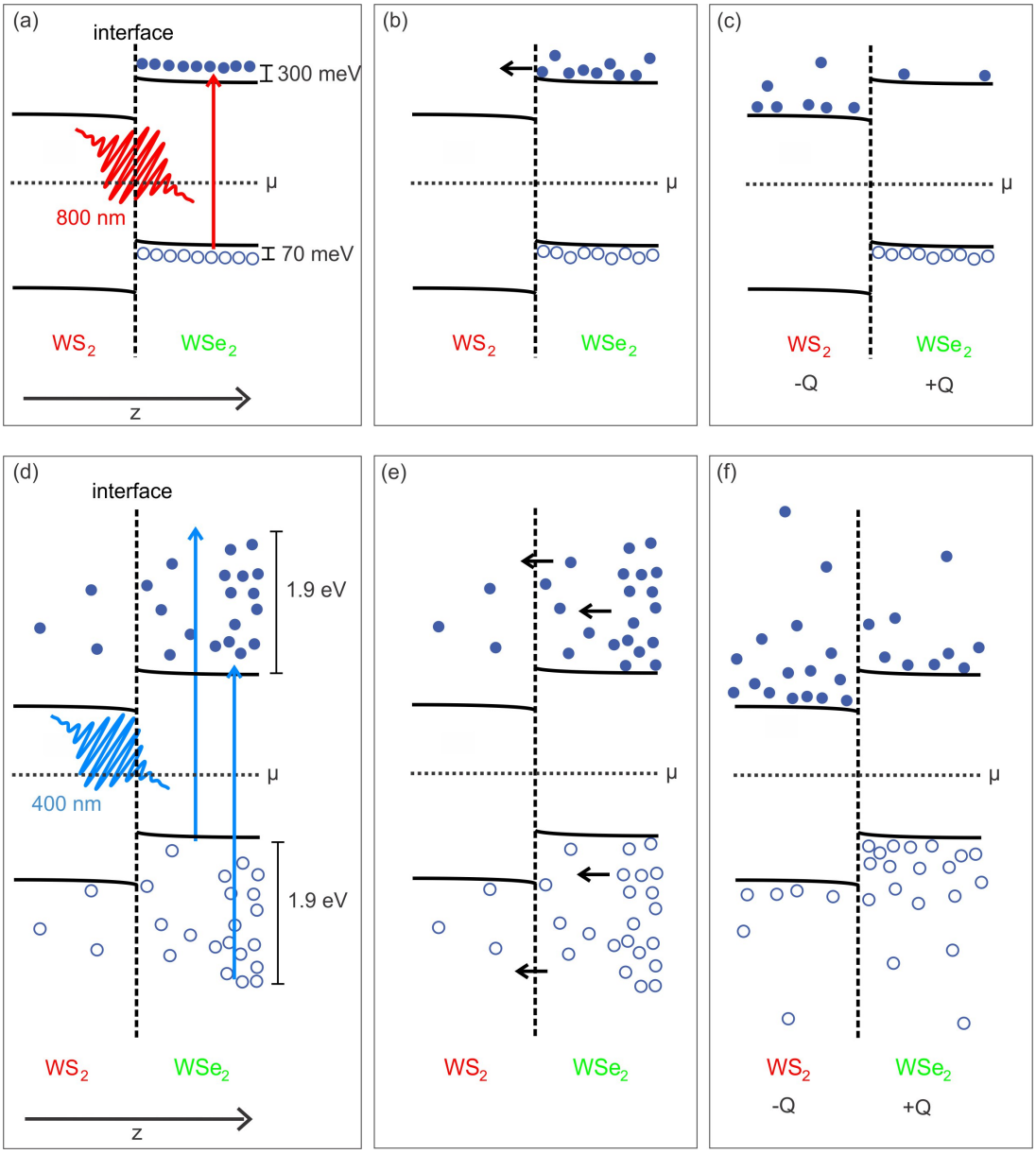

Figure 39: Comparison of the initial excitation condition and carrier transfer dynamics in the heterostructure for 800 nm and 400 nm excitation. Panel (a) illustrates the initial hot carrier distribution for 800 nm excitation. Carriers are excited almost uniformly in WSe_2. The excited carriers have energies close to the band edges of WSe_2. Panel (b) illustrates that only electrons can transfer to WS_2 due to the type-II band alignment. Panel (c) shows that after the transfer, WSe_2 is negatively charged and WS_2 is positively charged. Panel (d) depicts the initial hot carrier distribution for 400 nm excitation. Electrons are excited up to energies well above the conduction band minimum of WSe_2. Due to the short penetration depth, the excited carrier density is much higher close to the surface of WSe_2. Panel (e) shows that carrier-carrier scattering leads to a transport of electrons and holes towards and across the interface. In contrast to 800 nm excitation, both electrons and holes can cross the interface. Panel (d) shows that transfer and carrier-carrier thermalization lead to a charge imbalance between the two materials. WS_2 gets negatively charged and WSe_2 gets positively charged.

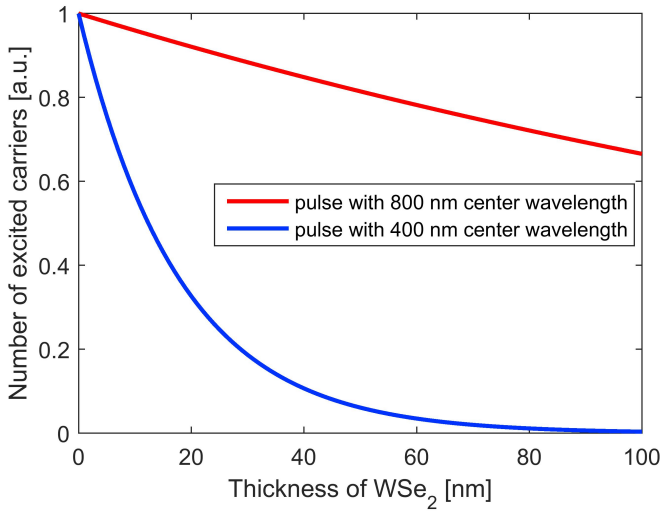

Figure 40: Comparison of the excitation profiles in WSe_2 for the pulses used in the time-resolved diffraction experiments. The number of carriers excited by the 400 nm pulses decays to half of the initial value within 12 nm. For the 800 nm pulses, this takes 190 nm (values are obtained from single-exponential fits of the curves). The calculation of the excitation profile is based on the optical constants by reference [Eic14]. The number of excited carriers in arbitrary units corresponds to the derivative of the intensity in the sample.

The observation of a different behavior for the two excitation conditions indicates that the electronic transfer across the interface can be fast in some cases. Nevertheless, there is a mechanism that delays the transfer in the case of excitation with 800 nm. In principle, efficient interfacial charge transfer on time scales much lower than 1.3 ps is a plausible result: The transfer can be achieved by scattering of an electron from a state located in WSe_2 into a state located in WS_2. It is plausible that this scattering process happens on time scales similar to electron-electron scattering. States that couple strongly in the z-direction could even hybridize to form states delocalized over the entire structure. In this case, the 'transfer' from WSe_2 to WS_2 is caused by the time-evolution of the initially prepared state, which causes the electronic density to spread across the sample. This process is also fast compared to the electron-lattice equilibration. Furthermore, the observation of efficient charge transfer agrees well with reports of sub-100 fs interlayer charge transfer in similar TMDC heterostructures [Hon14], [Zhu15], [Che16].

The observation of a delayed interfacial charge transfer for excitations with 800 nm can be explained by the presence of an energy barrier between the conduction band minimum of WSe_2 and the conduction band states in WS_2. Such an energy barrier would especially affect the dynamics of electrons excited with 800 nm wavelength due to their relatively low temperature. There probably is a small static energy barrier on the order of 5 meV or less that separates the states of WS_2 due to static band bending (compare Section 2.4.1). However, it is unlikely that such a small barrier has a significant effect on the electronic transfer efficiency. However, as discussed above, transient charge transfer leads to a charge imbalance between the materials. Both for 800 nm and 400 nm excitation, carrier-carrier scattering and interfacial transfer leads to surplus electrons in WS_2 and surplus holes in WSe_2. The charge separation causes an additional electrostatic potential, which influences the energy of the bands (transient band bending). This effect will be discussed in the following section.

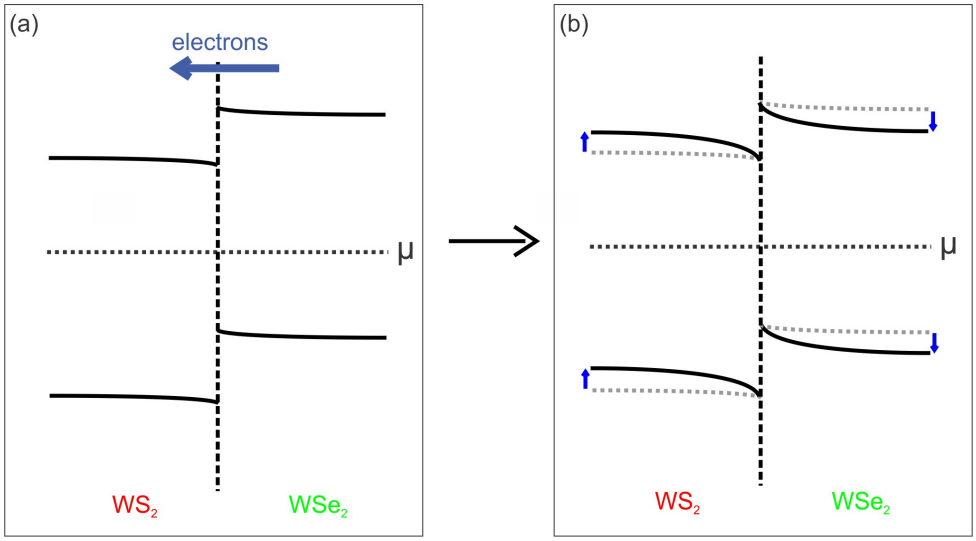

Figure 41: Illustration of transient band bending caused by charge transfer. If more electrons are transferred to WS_2 than holes are transferred to WSe_2, the charge imbalance between the material leads to transient band bending. Panel (a) shows the static situation before the pump pulse has arrived. Panel (b) illustrates the band bending diagram after transient electron transfer to WS_2.

7.2 Transient band bending

Both for 800 nm and 400 nm excitation, a charge imbalance is expected to develop. This transiently creates an additional electric field, which implies an additional potential. Hence, it changes the energetic positions of the bands, just as in the case of static charge transfer (compare Section 2.4.1). Qualitatively, the transient band shift has the same direction as the static band shift: The bands of WS_2 are shifted further upwards and the magnitude of the band bending increases. However, the transient band shift is much bigger than the static one because the number of excited carriers in the pumped sample is much higher than the number of thermally excited carriers at room temperature.

Figure 41 illustrates the transient band bending effect. The bands of WSe_2 are transiently bent upwards, which causes an energy barrier to develop between the conduction band minimum of WSe_2 and the states in WS_2. In the following, we estimate the density of excited carriers for which the magnitude of the band bending becomes significant. For simplicity, we assume the surplus charge to be distributed uniformly in the two materials. Furthermore, we assume the thicknesses of WS_2 and WSe_2 to be equal. Figure 42 schematically depicts the charge distribution in this case. Additionally, the figure shows the electric field and the additional energy of the electrons caused by this charge distribution.

If the charge distribution is known, the potential can be calculated using the Poisson equation. The details of the calculation for a constant charge distribution are in Appendix C. In this case, the potential energy depends quadratically on the position, as sketched in Figure 42 (c). The transient potential, measured from the interface, is:

$$|\Phi_{\text{transient}}| = \frac{1}{2}\frac{\rho_{\text{excess}}}{\epsilon_0} z^2 \tag{25}$$

ρ_{excess} is the density of the excess charge. Figure 43 displays the calculated electrostatic potential as a function of the distance from the interface and of the density of excited carriers. Already for charge densities of $10^{17}\frac{1}{\text{cm}^3}$, the magnitude of the electrostatic potential

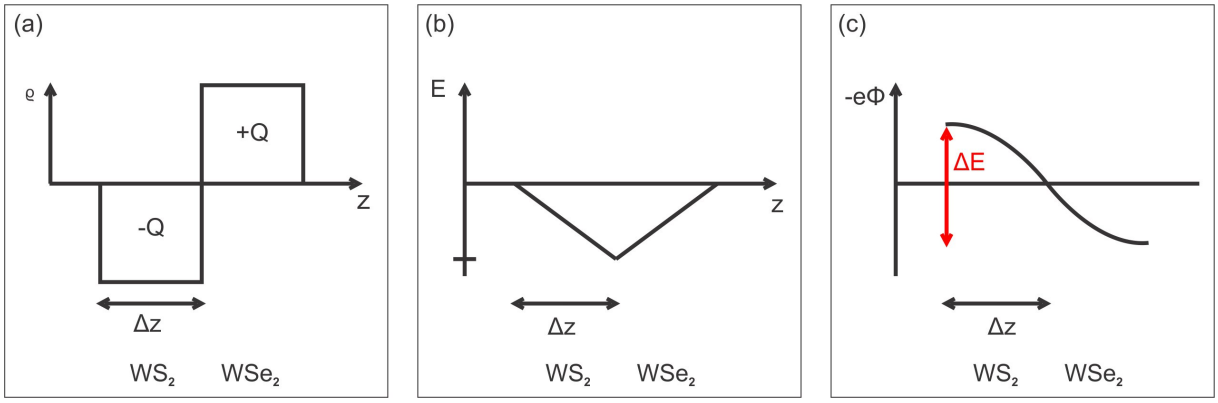

Figure 42: Illustration of the electrostatic potential due to charge imbalance between the two materials of the heterostructure. For simplicity, a constant charge distribution is assumed, which is shown in Panel (a). Panel (b) displays the electric field caused by the charge distribution. Panel (c) shows the resulting electrostatic potential.

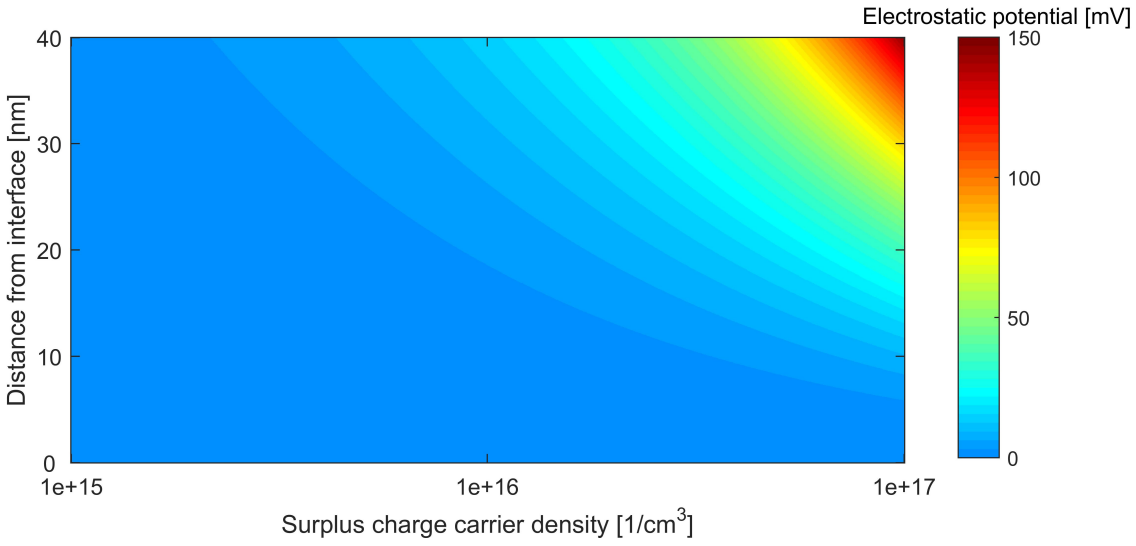

Figure 43: Resulting electrostatic potential for a constant distribution of the surplus charge (compare Figure 42 and Equation 25) as function of the density of surplus carriers and of the distance from the interface. The potential is measured with respect to the interface. See appendix for details on the calculation.

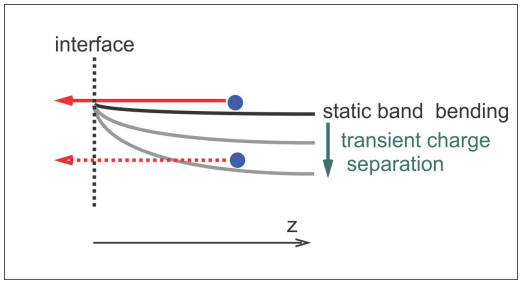

Figure 44: Illustration of the development of a transient energy barrier in the conduction band of WSe_2 after charge separation. Initially, there is only a negligibly small band bending and electrons in the conduction band of WSe_2 can transfer to WS_2 (solid red arrow). After transient charge separation, the amount of band bending increases significantly. This creates an energy barrier for electrons close to the conduction band minimum. The transient energy barrier can delay or even inhibit further carrier transfer (dashed red arrow).

is on the order of the band offsets at the junction (300-350 meV, compare Figure 7). In a typical pump-probe diffraction experiment, the excited charge carrier density is much higher, on the order of $10^{20} \frac{1}{\text{cm}^3}$. Consequently, we expect large transient band bending for all the experiments performed in this work. More precisely, the transient band bending reaches the saturation limit. In this limit, further charge separation is no longer energetically favorable.

To understand the difference between excitation with 800 nm and 400 mn, the energy of the excited carriers has to be considered: Carriers excited with λ=400 nm have large initial excess energies, up to 1.9 eV in WSe_2. In contrast, carriers excited with λ=800 nm have very little average excess energies. Electrons have initial excess energies of around 300 meV [Ber16]. Holes have even less excess energies, about 70 meV [Ril14]. As discussed above, transient band bending causes the bands of WSe_2 to shift upwards. This corresponds to an energy barrier that electrons in WSe_2 have to cross in order to transfer to WS_2. Figure 44 illustrates the formation of this energy barrier. In the saturation limit, the height of the energy barrier is on the order of 300-350 meV (the band offsets between the two materials). Since carriers excited with 400 nm have large initial excess energies, the energy barrier does not have a noticeable effect on the transfer. In contrast, for electrons excited with 800 nm, the transient energy barrier is high enough to delay the carrier transfer to WS_2.

To summarize, we attribute the slow energy transfer to WS_2 in the 800 nm case to the development of a transient energy barrier. The small excess energy of the electrons causes carrier transfer across the barrier to be relatively inefficient. This leads to a delayed carrier transfer across the interface.

7.3 Charge transport in WSe_2 and across the heterojunction

The 400 nm diffraction experiments on heterostructures as well as the optical experiments on WSe_2 indicate that the carrier transport in WSe_2 is efficient. This is remarkable since the charge is transported perpendicular to the layers (along the c-axis), which is typically the least conductive in layered materials [KK82]. In order for the carrier transport to be efficient, significant electronic coupling must exist between the layers. The strength of the interlayer coupling depends on the position of the electrons in k-space: positions where the dispersion varies significantly in k_z indicate strong interlayer coupling, or three-

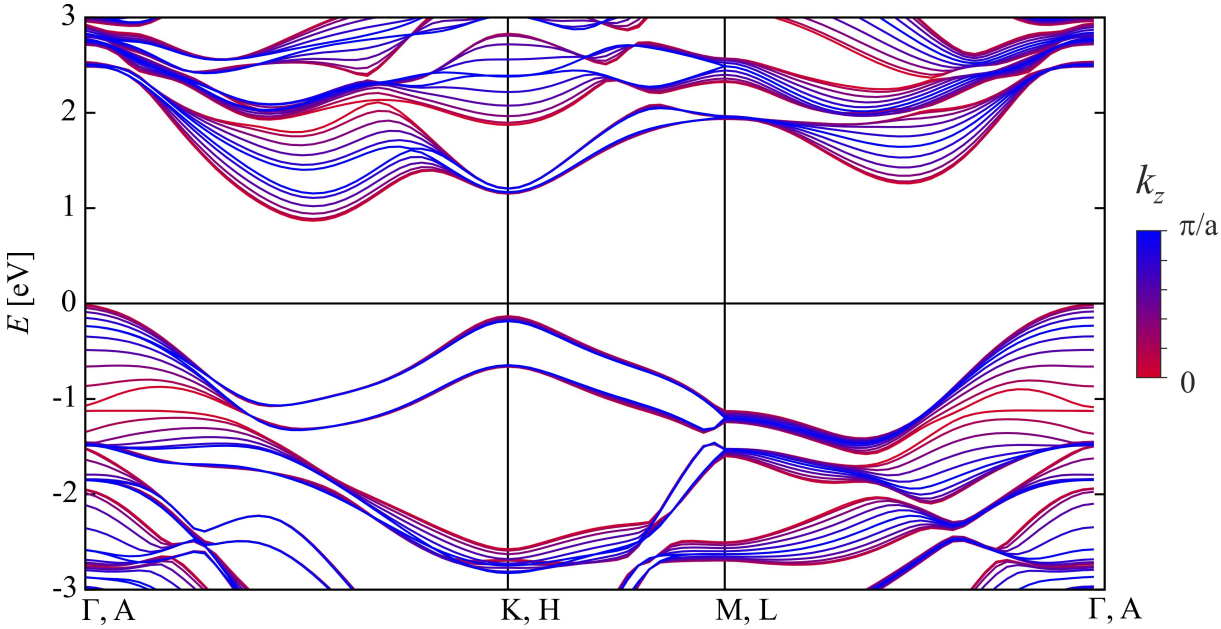

Figure 45: DFT calculation of the electronic structure of WSe_2 for k_z=0 (center of the Brillouin zone in z-direction) to $k_z = \frac{\pi}{a}$ (edge of the Brillouin zone in z-direction). States along K-H show a flat dispersion in z while states at Σ and Γ have a pronounced z-dispersion. From [Ber16].

dimensional character of the states. A flat dispersion in this direction indicates weak coupling / two-dimensional character. Figure 45 shows the electronic band structure of WSe_2 for different k_z.

In the optical experiments on WSe_2, which were performed using a pump center wavelength of 800 nm, the excitation happens at only one region of the Brillouin zone. Therefore, the states that are involved in the charge transport are known. The initial excitation happens at the K-point. According to their z-dispersion, states at the K-point are rather two-dimensional and thus couple weakly across the interface. The two-dimensionality is also reflected in the electron density distribution: Figure 46 shows A real-space image of the electron density for a conduction band state at the K-point. The electron density is high at the center of the layer, but low in between adjacent layers. This suggest weak coupling across the interface. Consequently, transport in the z-direction is expected to be inefficient for electrons at the K-point. However, in bulk WSe_2, the K-point is not the global minimum: The Σ-valley lies ca 300 meV below the K-valley [Ber16] (compare Figure 45). From time- and angle-resolved photoemission experiments, it is known that the electrons excited to the K-valley scatter to the Σ-valley within about 50 fs [Ber16]. In contrast to the rather two-dimensional K-states, the Σ-states are more three-dimensional: They have significant electron density in between the layers (compare Figure 46) and a high dispersion in k_z (compare Figure 45). Consequently, after scattering of electrons into the Σ-valley, transport along the z-direction is expected to be efficient.

Additionally, holes also contribute to the charge transport. Just like the conduction band states at the K-point, also the valence band states at this point are rather two-dimensional states with weak interlayer coupling. However, the global maximum of the valence band lies at the Γ-point [Ril14]. The states along Γ-A exhibit a pronounced dispersion in k_z and thus couple strongly between the layers. Consequently, holes are also expected to contribute significantly to the transport of excited carriers in the z-direction.

Based on these considerations, we conclude that the efficient carrier transport in WSe_2

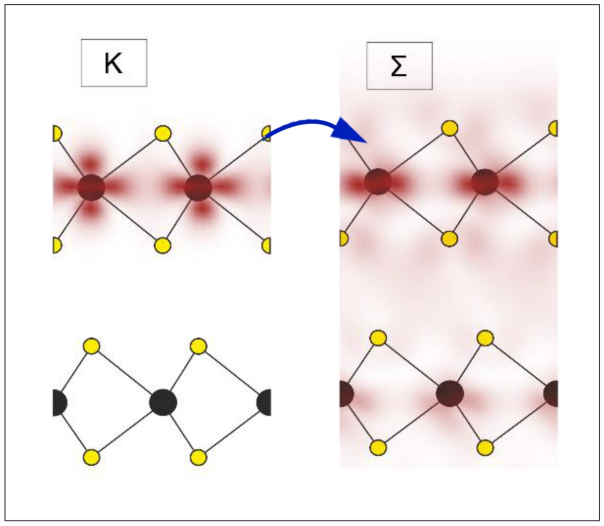

Figure 46: Real-space electron density distributions for a conduction band state at the K- and Σ-point, respectively. The K-state is rather two-dimensional with a low electron density between the layers. In contrast, the Σ-state has significant electron density between the layers and thus the interlayer coupling is stronger. Modified from reference [Ber16].

after 800 nm excitation is due to the scattering of hot carriers from two-dimensional into three-dimensional states. These three-dimensional states couple strongly in the direction perpendicular to the crystal layers.

In contrast, 400 nm pulses can excite many transitions. Figure 45 shows that there are several higher-lying states with a pronounced dispersion in k_z. Hence, the transport of excited carriers along the z-direction is expected to be efficient for this excitation condition as well. This agrees with the experimental observations.

The two- or three-dimensional character of the electronic states does not only influence the transport within the material, but also across the interface. The interlayer coupling influences the efficiency of the carrier transfer across the interface. In the case of bulk WSe_2, the conduction band minimum is at the Σ-point, which is a state with strong interlayer coupling. Also in WS_2, states with three-dimensional character exist at this energy. Consequently, efficient carrier transfer is expected.

On the other hand, in TMDC monolayers, the conduction band minimum is at the K-point, which has two-dimensional character. Nevertheless, sub-100 fs charge transfer has been observed for monolayer-monolayer heterostructures as well [Hon14], [Zhu15], [Che16]. Consequently, the interfacial transfer is expected to be even more efficient in the case of bulk TMDC heterostructures. This is consistent with the observation of the fast carrier transfer across the interface in the case of 400 nm excitation.

7.4 Carrier-lattice energy transfer and phonon thermalization in the individual materials

So far, we have discussed electronic transfer across the interface and electron-electron scattering processes. These processes only establish equilibrium within the electronic subsystem. On longer time scales, energy is transferred from the excited carriers to the lattice. To study the lattice dynamics in the individual materials, we perform measurements on a WSe_2 and a WS_2 sample using 400 nm excitation wavelength. In both cases, the Bragg peak attenuation is described well by a single-exponential behavior with a time

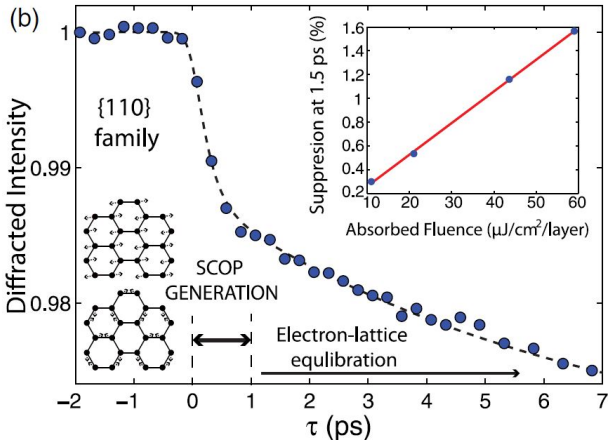

Figure 47: Bragg-peak attenuation of graphite after 800 nm excitation, probed with 80 keV-electrons at normal incidence. A biexponential behavior is observed: The excited electrons couple strongly to optical phonons, causing the initial decay. The second decay with a much longer time constant corresponds to the decay of optical phonons into acoustic phonons. From [Cha14].

constant of around 1.3 ps.

In general, the relaxation of carriers towards the band edges produces a nonequilibrium phonon distribution. The number of phonons created in a certain mode depends on the matrix elements for electron-phonon coupling and on the available phase space. Often, the coupling to optical phonons is larger than to acoustic phonons [Wal16a], [Cha14]. If the coupling to optical phonons is much larger, it can result in a biexponential Bragg peak decay: First, a large number of optical phonons is created. Recalling the discussion of Section 3.3, optical phonons have only a small effect on the Bragg peak attenuation compared to acoustic phonons. On longer time scales, the number of optical phonons decreases as the phonon distribution thermalizes and more acoustic phonons are created. This results in a second time scale for the Bragg peak attenuation. In total, a biexponential behavior is observed. For example, this is the case for graphite [Cha14]. Figure 47 shows a time trace of its Bragg peak attenuation.

In contrast, in the experiments on WSe_2 and WS_2, a single-exponential behavior is observed, even though it is known that it takes several tens of picoseconds until the phonon distribution is fully thermalized [Wal17]. To interpret this result, it is important to keep in mind that in the experiment, only in-plane modes are observed. In WSe_2, the coupling to the optical phonon branches B_{2g} and A_{2u} close to the Brillouin center is particularly high [Wal17]. At the zone center, these modes correspond to an out-of-plane vibration and are therefore not observed in the experiment. In principle, it is possible that the initially created optical phonons are mainly 'dark' for electron diffraction at normal incidence. In this case, the observed signal stems mainly from acoustic phonons created by phonon-phonon scattering. The scenario requires the decay of optical phonons into acoustic phonons to happen on a timescale of 1.3 ps, which is rather fast for phonon-phonon coupling. On the other hand, it is known that the phonon-phonon equilibration between phonons with different momenta takes several tens of picoseconds [Wal17]. Therefore, the decay of the optical phonons into acoustic phonons would have to be much more efficient than the equilibration between acoustic phonons with different momenta.

Another possibility is that the number of acoustic phonons created during carrier

relaxation is larger than the number of optical phonons. This could be caused by phase space effects, since carriers close to the band edges can only create acoustic phonons.

In summary, from the measurements on free-standing WSe_2 and WS_2 we are able to determine the time constant for the carrier-lattice energy transfer: (1.3±0.1) ps for WSe_2 and (1.3±0.2) ps for WS_2. These values should be seen as an upper limit, since phonon-phonon scattering processes can also contribute to the observed dynamics.

7.5 Equilibration between the two materials

As discussed above, electronic coupling is the fastest mechanism that transfers energy between the two materials. However, due to the different band structures of the two materials, transfer and relaxation of carriers does not necessarily lead to the same lattice temperature in both materials. In a situation where the lattice temperatures are different, equilibration will eventually be restored by vibrational coupling across the interface, which typically takes place on a timescale of tens of picoseconds or more. We measure the structural dynamics after 400 nm excitation up to a time delay of 1 ns (compare Figure 27). No further energy transfer processes at long time delays are observed. Equilibrium between the two materials is already established after less than 10 ps.

One explanation for this observation is that the excited carriers distribute their energy approximately equally in the two materials. In this case, the temperature difference between the two lattices is small. This is a plausible scenario for the dynamics after 400 nm excitation: As already discussed in Section 7.2, the excess energy of the carriers in WSe_2, up to 1.9 eV, is much higher than the magnitude of the transient band bending. Hence, the interfacial transfer is efficient. In this case, the energy deposited in each material depends mainly on the average excess energy of the carriers in the respective material. The average excess energy is determined by the photon energy and indirect band gaps. WSe_2 has an indirect band gap of 1.2 eV [Yeh15] and WS_2 has an indirect band gap of 1.35 eV [Bra12]. Since the difference is small, much smaller than the carrier excess energy, the amount of energy (per volume) transferred to the lattice is expected to be approximately the same for the two materials. Furthermore, also their heat capacities are similar: WSe_2 has a heat capacity of $c_p = 72 \frac{\mathrm{J}}{\mathrm{mol\ K}}$ [Bol90] and WS_2 has a heat capacity of $c_p = 64 \frac{\mathrm{J}}{\mathrm{mol\ K}}$ [o'H84]. Hence, the lattice temperatures are expected to differ little after electron-lattice equilibration. This can explain the absence of energy transfer processes at long time delays.

Furthermore, even if there is a temperature difference between the two materials, vibrational coupling between them is probably very slow, as already discussed in Section 2.3. This is due to the low overlap between the phonon dispersions of the materials (compare Figure 5 of Section 2.3). Consequently, even if there is a slight temperature difference, it is probably not resolved in the measurements: in the time traces, the equilibration would appear as a small difference in the slope of the two curves, which is difficult to detect due to the noise of the signal.

8 Summary and Outlook

We investigate the structural dynamics of bulk WS_2/WSe_2 heterostructures after photoexcitation using time-resolved electron diffraction. This technique probes transient changes in the phonon population after photoexcitation by making use of the Debye-Waller-effect. By using single crystals, it is possible to observe the response of the two materials separately and thus study electronic and vibrational coupling across the interface. We used two different excitation wavelengths, 400 nm and 800 nm, to create two different initial carrier distributions in the heterostructure: Exciting the sample with 400 nm creates electrons with energies well above the conduction band minimum (and holes well below the valence band maximum). Furthermore, most free carriers close to the interface of WSe_2. After excitation, we observe a significant carrier transfer across the interface. It is is efficient enough such that we observe no delay of the carrier-lattice energy transfer in WS_2. The carrier transfer thus happens on time scales significantly shorter than 1.3 ps, in agreement with previous results [Hon14] [Zhu15], [Che16], [Pan16]. Additionally, fluence-dependent diffraction experiments on the heterostructure show that no saturation effects occur for the carrier transfer to WS_2.

Also within WSe_2, the charge transfer is very efficient. This result is confirmed by optical front pump / back probe experiments on WSe_2, which yield a rough estimate for the transport velocity on the order of 10 $\frac{nm}{fs}$.

In contrast, 800 nm excitation creates a spatially quite homogeneous density of carriers in WSe_2. Due to the low photon energy, all carriers are located close to the band edges. WS_2 is almost not excited. For this excitation condition, we also observe charge transfer to WS_2. However, the time constant for the energy transfer to the lattice of WS_2 is significantly larger than the time constant of WSe_2. This indicates that the carrier transfer to WS_2 is slow enough to significantly delay its structural response. We attribute the delayed transfer to the development of a transient energy barrier after electron transfer. This effect could be studied further by recording fluence-dependent measurements. From the estimations of the transient band bending presented in Section 7.2, we inferred that for typical excitation densities, saturation of the charge separation is already reached. In this limit, the time constant of WS_2 as well as the amount of transferred charge is expected to be independent on the fluence. Hence, fluence-dependent measurements could yield further information on the transient band bending. However, such experiments require very stable experimental conditions. The noise level of the 800 nm experiments is quite high and thus good statistics is necessary. Additionally, to monitor the transferred charge independently on assumptions about the initial excitation profile, reference measurements on free-standing WSe_2 could be recorded, just as in the case of 400 nm excitation (compare Figure 28).

Furthermore, the influence of transient energy barriers on the carrier transfer could also be investigated by using doped crystals: In particular, p-doping of WS_2 and n-doping of WSe_2 would increase the amount of carriers that flow across the interface upon contact. Hence, the static band bending would be much higher compared to undoped crystals. Figure 48 shows the band bending diagram for doped crystals. By comparing the relaxation behavior of heterostructures with different dopant concentrations, the influence of band bending effects on the carrier transfer across the interface could be studied further.

Additionally, further information on the heterostructure could be gained by investigating its behavior at long time delays for different excitation conditions. In general, interfacial carrier transfer and carrier-lattice equilibration does not necessarily lead to the

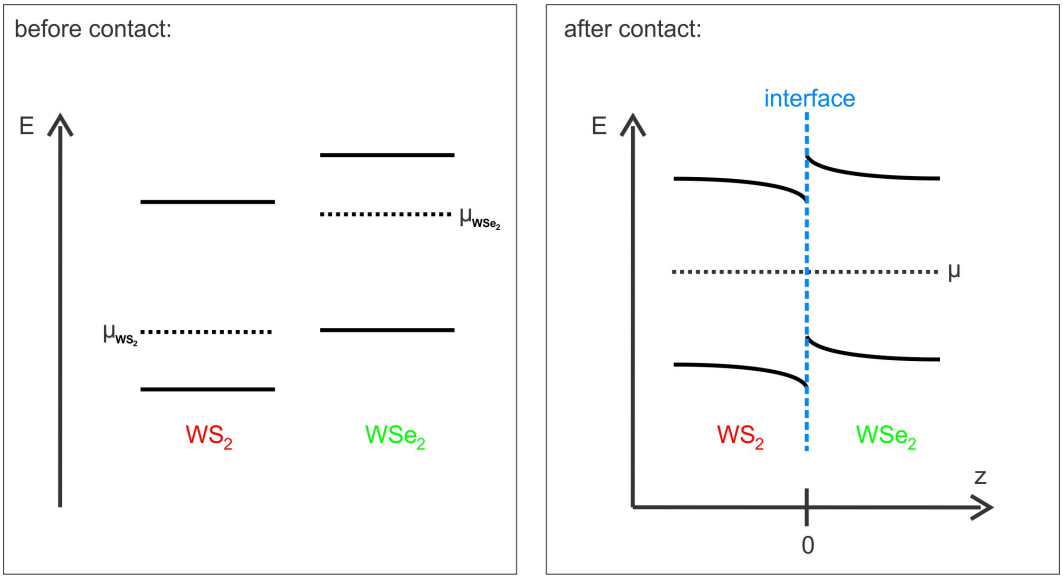

Figure 48: Band bending in the case of p-doped WS_2 and n-doped WSe_2. Compared to the undoped heterojunction, the band bending is much higher due to the large number of electrons in the conduction band of WSe_2 and the large number of holes in the valence band of WS_2.

equilibration of the two materials. The amount of energy transferred to the lattice depends on the carrier number and energy in each material. If there is still a non-equilibrium between the two materials after carrier transfer and carrier-lattice-equilibration, further energy is transferred across the interface by vibrational coupling. These processes can also be detected in time-resolved diffraction. For 400 nm excitation wavelength, no energy transfer at long time scales is observed. We attribute this to the very similar indirect band gaps of the two materials, which differ only by about 150 meV. Given that the carriers excited with 400 nm have high excess energies of up to 1.9 eV, the amount of energy per volume transferred to each material is expected to be roughly the same. This could be different for 800 nm excitation: First, carriers have small excess energies. Thus, the indirect band gap difference of 150 meV is more relevant. Second, the interfacial charge transfer is delayed by the transient energy barrier. Consequently, the two lattice temperatures could be different after electron-lattice thermalization.

The efficiency of the interfacial heat transfer depends on the overlap of the phonon dispersions (compare Section 2.4.2) and thus on the alignment of the two crystals. If vibrational coupling is observed in the 800 nm case, in the next step, the dependence of the coupling on the rotation angle could be studied.

Vibrational coupling could also be studied in systems in which excited carrier transfer across the interface is not possible. For this, a semiconductor heterostructure with straddling (type I) band alignment is required. Furthermore, the bandgaps need to differ in order to be able to selectively excite one of the two materials. Alternatively, a semiconductor/metal heterojunction is also suitable. Hence, possible choices include for example WSe_2 and hexagonal boron nitride (hBN), or graphene and hBN. Figure 49 displays the band alignment of these heterostructures. Since the lattice temperature of hBN can only rise by vibrational heat transfer, these systems have the advantage that vibrational coupling can be studied isolated from other effects.

In conclusion, our experiments show that time-resolved electron diffraction on heterostructures is a tool that allows to study not only the structural dynamics within the

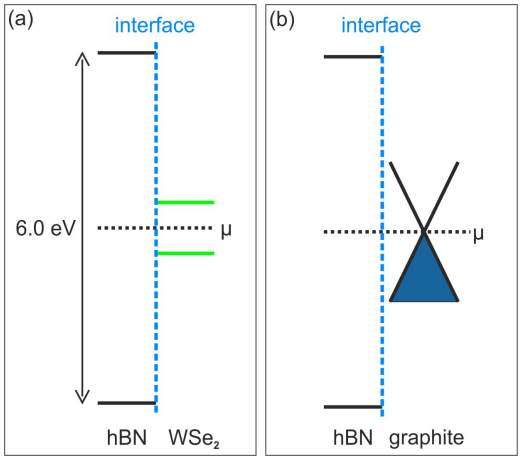

Figure 49: Panel (a) shows the band alignment of a hexagonal boron nitride (hBN)/WSe_2 heterostructure (multilayer/multilayer). The heterostructure exhibits a straddling (type I) band alignment. Panel (b) shows the band alignment of a hBN/graphene heterostructure (multilayer/monolayer). Both heterostructures can be used to study vibrational coupling across the interface by exciting only WSe_2 or graphene, respectively. The band bending is negligible for typical sample thicknesses (tens of nanometers) due to the very low density of excited carriers in hBN.

individual materials, but also both electronic and vibrational energy transfer processes across heterostructure interfaces. In principle, any sample consisting of two or even more single-crystalline materials can be studied. Consequently, the technique could help to shed light on electronic and thermal interfacial coupling in a large number of different heterojunctions. Understanding these interactions is a first step towards the successful design of devices based on two-dimensional van der Waals materials.

Appendix A: transmission measurements with the optical microscope

To estimate the accuracy of the transmission measurement described in Section 4.3, we measured the density of several ND filters (Thorlabs NEXXA, XX=OD*10). The resulting values are:

optical density	filter	expected transmittance	measured transmittance	deviation
0.3	none	0.50	0.50	0%
	406-422 nm	0.49	0.50	+2%
	628-672 nm	0.50	0.55	+10%
	773-812 nm	0.47	0.53	+13%
0.5	none	0.32	0.29	-10%
1	none	0.11	0.10	-9%
	406-422 nm	0.10	0.08	-20%
	628-672 nm	0.10	0.11	+10%
	773-812 nm	0.14	0.17	+21%

In general, the measured transmission values agree well with the expected ones. The accuracy of the method is about 10 % for transmission of 0.3 or more and around 20 % for smaller values.

The limited accuracy of these values leads to a rather large uncertainty of the calculated thicknesses. Furthermore,literature values for the optical properties don't always agree. This also contributes to the uncertainty of the flake thicknesses determined by this method.

A more precise determination of the thickness could be achieved by measuring transmission and/or reflection spectra locally. This method has the advantage that the interference features could be identified and used for the determination of the sample thickness. The position of the interference peaks only depends on the sample thickness, but not on the optical properties. Consequently, a much more precise determination of the thickness would be possible with this method.

Appendix B: properties of the heterostructure samples

The time-resolved diffraction measurements were taken on three different WS_2/WSe_2 heterostructure samples. The thicknesses of the constituent materials were determined using the method described in Section 4.3. Using this information and the optical properties of WSe_2 and WS_2 [Bea76], [Eic14], the ratio of energy deposited in each material for excitation with 400 nm center wavelength was calculated. The results are displayed below.

sample	d_{WSe_2} [nm]	d_{WS_2} [nm]	$\langle E_{WSe_2}\rangle$ / $\langle E_{WS_2}\rangle$ (total energy)	$(d_{WS_2} \cdot \langle E_{WSe_2}\rangle)/(d_{WSe_2} \cdot \langle E_{WS_2}\rangle)$ (energy per layer)
1	39±10	10±5	≥89%	≥75%
2	40±10	30±5	≥87%	≥83%
3	26±5	12±3	≥82%	≥72%

Samples 1 and 2 were used for the measurements with 400 nm pump center wavelength. The ratio of energy deposited per layer in WSe_2 compared to WS_2 is high for both these samples. This result is important for the experiments with 400 nm excitation wavelength: It allows to conclude that the Bragg peak attenuation of WS_2 is mainly due to electrons transferred across the interface (compare Section 7.1). Sample 3 was used for the measurements with 800 nm pump center wavelength.

Appendix C: calculation of the potential offset due to static and transient charge imbalance

As explained in sections 2.4.1 and 7.2, charge imbalance between the materials creates an electrostatic potential. This leads to energetic shifts of the bands and can be visualized using a band bending diagram (compare figures 7 and 41). The electrostatic potential depends on the distribution of the excess charge in each material, which is often unknown. A simple estimation can be made based on the assumption of a homogeneous charge distribution (compare Figure 42 a). Let ρ be the surplus charge density. For a homogeneous distribution of the surplus charge carriers within a thickness d on each side, it reads:

$$\rho(z) = \begin{cases} -\rho_0 & \text{if } -d < z < 0 \\ \rho_0 & \text{if } 0 < z < d \\ 0 & \text{otherwise} \end{cases} \tag{26}$$

d is the thickness of the two materials forming the heterojunction. For simplicity, we assume the same thickness for both materials. We also assume the heterojunction to extend infinitely in x- and y direction, which is an excellent approximation for the heterostructures studied in this work. Then, we can treat the problem as being one-dimensional. In order to obtain the potential, the 1-D Poisson equation has to be solved:

$$\frac{\partial^2 \Phi(x)}{\partial^2 z} = \frac{\rho}{\epsilon_0} \tag{27}$$

ϵ_0 denotes the vacuum permittivity. The above equation can be solved by integrating twice. The first integration yields:

$$E(x) = \frac{\partial \Phi}{\partial x} = \begin{cases} -\frac{\rho_0}{\epsilon_0} x & \text{if } -d < z < 0 \\ \frac{\rho_0}{\epsilon_0} x & \text{if } 0 < z < d \end{cases} \tag{28}$$

Here, the boundary condition $E(-d) = E(d) = 0$ was already inserted[11]. The second integration results in the expression for the potential:

$$\phi(x) = \begin{cases} -\frac{1}{2}\frac{\rho_0}{\epsilon_0} d^2 & \text{if } z < -d \\ -\frac{1}{2}\frac{\rho_0}{\epsilon_0} x^2 & \text{if } -d < z < 0 \\ \frac{1}{2}\frac{\rho_0}{\epsilon_0} x^2 & \text{if } 0 < z < d \\ \frac{1}{2}\frac{\rho_0}{\epsilon_0} d^2 & \text{if } z < -d \end{cases} \tag{29}$$

This expression was used to estimate the amount of static and transient band bending.

[11] This can be derived using Gauss law. The situation is very similar to the case of a parallel plate capacitor.

References

[And62] R.L. Anderson. *Experiments on the Ge-GaAs heterojunction.* Solid State Electronics 5, 341–351 (1962).

[Bas64] D. C. Bassett. *On moiré patterns in the electron microscopy of polymer crystals.* Philosophical Magazine 10, 595–615 (1964).

[Bea76] A. R. Beal, W. Y. Liang, & H. P. Hughes. *Kramers-Krönig analysis of the reflectivity spectra of 3R-WS_2 and 2H-WSe_2.* Journal of Physics C: Solid State Physics 9, 2449–2457 (1976).

[Ber] R. Bertoni. *Electron lattice interactions in bulk WSe_2 probed by ultrafast electron diffraction.* In preparation.

[Ber16] R. Bertoni, C.W. Nicholson, L. Waldecker, H. H'ubener, C. Monney, U. de Giovannini, M. Puppin, M. Hoesch, E. Springgate, R.T. Chapman, C. Cacho, M. Wolf, A. Rubio, & R. Ernstorfer. *Generation and evolution of spin-, valley- and layer-polarized excited carriers in inversion-symmetric WSe_2.* Physical Review Letters 117, 277201 (2016).

[Boe64] H. Boersch, O. Bostanjoglo, & H. Niedrig. *Temperaturabhängigkeit der Transparenz dünner Schichten für schnelle Elektronen.* Zeitschrift für Physik 180, 407–414 (1964).

[Bol90] A. S. Bolgar, Zh. A. Trofimova, & A. A. Yanaki. *Thermodynamic properties of tungsten diselenide in a broad temperature range.* Soviet Powder Metallurgy and Metal Ceramics 29, 382–385 (1990).

[Bra12] D. Braga, I. G. Lezama, H. Berger, & A. F. Morpurgo. *Quantitative determination of the band gap of WS_2 with ambipolar ionic liquid-gated transistors.* Nano Letters 12, 5218–5223 (2012).

[Bro62] S. D. Brorson, J. G. Fujimoto, & E. P. Ippen. *Femtosecond electronic heat-transport dynamics in thin gold films.* Physical Review Letters 59, 1962–1965 (1962).

[Bro06] P.J. Brown, A.G. Fox, E.N. Maslen, M.A. O'Keefe, & B.T.M. Willis. *International tables for crystallography*, Bd. C. Wiley, 2006.

[CG14] A. Castellanos-Gomez, M. Buscema, R. Molenaar, V. Singh, L. Janssen, H. S. J. van der Zant, & G. Steele. *Deterministic transfer of two-dimensional materials by all-dry viscoelastic stamping.* 2D Materials 1, 011002 (2014).

[Cha01] P. E. Champness. *Electron diffraction in the transmission electron microscope.* Taylor & Francis, 2001.

[Cha14] R. Chatelain, V. Morrison, B. Klarenaar, & B. J. Siwick. *Coherent and Incoherent Electron-Phonon Coupling in Graphite Observed with Radio-Frequency Compressed Ultrafast Electron Diffraction.* Physical Review Letters 113, 235502 (2014).

[Che15] A. Chernikov, C. Ruppert, H. Hill, A. Rigosi, & T. Heinz. *Population inversion and giant bandgap renormalization in atomically thin WS_2 layers.* Nature Photonics 9, 466–470 (2015).

[Che16] H. Chen, X. Wen, J. Zhang, T. Wu, Y. Gong, X. Zhang, J. Yuan, C. Yi, J. Lou, P. M. Ajayan, W. Zhuang, G. Zhang, & J. Zheng. *Ultrafast formation of interlayer hot excitons in atomically thin MoS2/WS2 heterostructures.* Nature Communications 7, 12512 (2016).

[Chi16] M.-H. Chiu, W.-H. Tseng, H.-L. Tang, Y.-H. Chang, C.-H. Chen, W.-T. Hsu, W.-Hao Chang, C.-I Wu, & L.-J. Li. *Band alignment of 2D transition metal dichalcogenide heterojunctions.* Advanced Functional Materials (2016).

[Dav72] B. Davey & B. L. Evans. *The optical properties of $MoTe_2$ and MoS_2.* Physica Status Solidi A: Applications and Materials Science 13, 483–491 (1972).

[Eic14] S.M. Eichfeld, C.M. Eichfeld, Y.-C. Lin, L. Hossain, & J.A. Robinson. *Rapid, non-destructive evaluation of ultrathin WSe2 using spectroscopic ellipsometry.* APL Materials 2, (2014).

[Flö15] N. Flöry, A. Jain, P. Bharadwaj, M. Parzefall, T. Taniguchi, K. Watanabe, & L. Novotny. *A $WSe_2/MoSe_2$ heterostructure photovoltaic device.* Applied Physics Letters 107, 123106 (2015).

[Gei07] A. K. Geim & K. S. Novoselov. *The rise of graphene.* Nature Materials 6, 183–191 (2007).

[Gei13] A. K. Geim & I. V. Grigorieva. *Van der Waals heterostructures.* Nature 499, 419–425 (2013).

[Hon14] X. Hong, J. Kim, S. F. Shi, y. Zhang, C. Jin, Y. Sun, S. Tongay, J. Wu, Y. Zhang, & F. Wang. *Ultrafast charge transfer in atomically thin MoS_2/WS_2 heterostructures.* Nature Nanotechnology 9, 682–686 (2014).

[Iba09] H. Ibach & H. Lüth. *Solid state physics: an introduction to principles of materials science.* Springer, 2009.

[Kan13] J. Kang, S. Tongay, J. Zhou, J. Li, & J. Wu. *Band offsets and heterostructures of two-dimensional semiconductors.* Applied Physics Letters 102, 012111 (2013).

[Kit05] C. Kittel. *Introduction to solid state physics.* Wiley, 2005.

[KK82] K. Kam-Keung. *Electrical properties of tungsten diselenide, tungsten disulfide, molybdenum diselenide, molybdenum disulfide and their use as photoanodes in a semiconductor liquid junction solar cell.* Dissertation, Iowa State university (1982).

[Kum12] A. Kumar & P. K. Ahluwalia. *Electronic structure of transition metal dichalcogenides monolayers 1H-MX2 (M = Mo, W; X = S, Se, Te) from ab-initio theory: new direct band gap semiconductors.* The European Physical Journal B 85, 18–22 (2012).

[Li13] Y. Li, Y Rao, K. F. Mak, Y. You, S. Wang, C. R. Dean, & T. F. Heinz. *Probing symmetry properties of few-layer MoS_2 and h-BN by optical second-harmonic generation.* Nano Letters 13, 3329–3333 (2013).

[Lig11] M. Ligges, I. Rajkovi, C. Streubhr, T. Brazda, P. Zhou, O. Posth, C. Hassel, G. Dumpich, & D. von der Linde. *Transient (000)-order attenuation effects in ultrafast transmission electron diffraction.* Journal of Applied Physics 109, 063519 (2011).

[Lui13] C. H. Lui & T. F. Heinz. *Measurement of layer breathing mode vibrations in few-layer graphene.* Physical Review B 87, 121404 (2013).

[MS11] A. Molina-Sánchez & L. Wirtz. *Phonons in single-layer and few-layer MoS_2 and WS_2.* Physical Review B 84, 155413 (2011).

[Nov04] K. S. Novoselov, A. K. Geim, S. Morozov, D. Jiang, Y. Zhang, S. Dubonos, I. Grigorieva, & A. A. Firsov. *Electric field effect in atomically thin carbon films.* Science 306, 666–669 (2004).

[Nov12] K. S. Novoselov, V. I. Fal'ko, L. Colombo, P. R. Gellert, M. G. Schwab, & K. Kim. *A roadmap for graphene.* Nature 490, 192–200 (2012).

[o'H84] P. A. G. o'Hare, W. N. Hubbard, G. K. Johnson, & H. E. Flotow. *Calorimetric measurements of the low-temperature heat capacity, standard molar enthalpy fo formation at 298.15 K, and high-temperature molar enthalpy increments relative to 298.15 K of tungsten disulfide (WS_2), and the thermodynamic properties to 1500 K.* The Journal of Chemical Thermodynamics 16, 45–49 (1984).

[Pan16] S. Pan, F. Ceballos, M. Z. Bellus, P. Zereshki, & H. Zhao. *Utrafast charge transfer between $MoTe_2$ and MoS_2 monolayers.* 2D Materials 4, (2016).

[Pen10] L. M. Peng, S. L. Dudarev, & M. J. Whelan. *High-energy electron diffraction and microscopy.* Oxford University Press, 2010.

[Pol12] A. Polman & H. Atwater. *Photonic design principles for ultrahigh-efficiency photovoltaics.* Nature Materials 11, 174–177 (2012).

[Pup] M. Puppin . Unpublished results.

[Pur16] A. A. Puretzky, L. Liang, X. Li, K. Xiao, B. G. Sumpter, V. Meunier, & D. B. Geohegan. *Twisted $MoSe_2$ bilayers with variable local stacking and interlayer coupling revealed by low-frequency Raman spectroscopy.* ACS Nano 10, 2736–2744 (2016).

[Ril14] J. M. Riley, F. Mazzola, M. Dendzik, M. Michiardi, T. Takayama, L. Bawden, C. Granerod, M. Leandersson, T. Balasubramanian, M. Hoesch, T.K. Kim, W. Takagi, H. an Meevasana, P. Hofmann, M. S. Bahramy, J. W. Wells, & P. D. C. King. *Direct observation of spin-polarized bulk bands in an inversion-symmetric semiconductor.* Nature Physics 10, 835–839 (2014).

[Roy15] T. Roy, M. Tosun, X. Cao, H. Fang, D. Lien, P. Zhao, Y. Chen, Y. Chueh, J. Guo, & A. Javey. *Dual-gated MoS_2/WSe_2 van der Waals tunnel diodes and transistors.* ACS Nano 9, 2071–2079 (2015).

[Sah13] H. Sahin, S. Tongay, S. Horzum, W. Fan, J. Zhou, J. Li, J. Wu, & F. M. Peeters. *Anomalous Raman spectra and thickness-dependent electronic properties of WSe_2.* Physical Review B 87, 165409 (2013).

[Swa89] E.T. Swartz & R.O. Pohl. *Thermal boundary resistance.* Review of Modern Physics 61, 605–668 (1989).

[Tan12] P. H. Tan, W. P. Han, W. J. Zhao, Z. H. Wu, K. Chang, H. Wang, Y. F. Wang, N. Bonini, N. Marzari, N. Pugno, G. Savini, A. Lombardo, & A. C. Ferrari. *The shear mode of multilayer graphene.* Nature Materials 11, 294–300 (2012).

[Ter14] H. Terrones, E. Del Corro, S. Feng, J. M. Poumirol, D. Rhodes, D. Smirnov, N.R. Pradhan, Z. Lin, M. A. T. T. Nguyen, A. L. Elías, T. E. Mallouk, L. Balicas, M. A. Pimenta, & M. Terrones. *New first order Raman-active modes in few layered transition metal dichalcogenides.* Scientific Reports 4, (2014).

[Wal16a] L. Waldecker, R. Bertoni, R. Ernstorfer, & J. Vorberger. *Electron-phonon coupling and energy flow in a simple metal beyond the two-temperature approximation.* Physical Review X 6, (2016).

[Wal16b] Lutz Waldecker. *Electron-lattice interactions and ultrafast structural dynamics of solids.* Dissertation, Freie Universität Berlin (2016).

[Wal17] L. Waldecker, R. Bertoni, H. Hübener, T. Brumme, T. Vasileiadis, R. Rubio, & R. Ernstorfer. *A momentum resolved view on electron-phonon scattering in multilayer WSe_2.* arXiv:1703.03496 (2017).

[War90] B. E. Warren. *X-ray diffraction.* Dover, 1990.

[Win98] D.L. Windt. *IMD - Software for modeling the optical properties of multilayer films.* Computers in Physics 12, 360 (1998).

[Xu05] R. Xu & T. C. Chiang. *Determination of phonon dispersion relations by X-ray thermal diffuse scattering.* Zeitschrift für Kristallographie 220, 1009–1016 (2005).

[Yeh15] P.-C. Yeh, W. Jin, N. Zaki, D. Zhang, J. T. Liou, J. T. Sadowski, A. Al-Mahboob, J. I. Dadap, I. P. Herman, P. Sutter, & Jr. R. M. Osgood. *Layer-dependent electronic structure of an atomically heavy two-dimensional chalcogenide.* Physical Review B 91, (2015).

[Zen13] H. Zeng, G.-B. Liu, J. Dai, Y. Yan, B. Zhu, R. He, L. Xie, S. Xu, X. Chen, W. Yao, & X. Cui. *Optical signature of symmetry variations and spin-valley coupling in atomically thin tungsten dichalcogenides.* Scientific Reports 3, (2013).

[Zha13] W. Zhao, Z. Ghorannevis, L. Chu, M. Toh, C. Kloc, P. H. Tan, & G. Eda. *Evolution of electronic structure in atomically thin sheets of WS_2 and WSe_2.* ACS Nano 7, 791–797 (2013).

[Zha15] X. Zhang, X. Qiao, W. Shi, J. Wu, D. Jiang, & P. Tan. *Phonon and Raman scattering of two-dimensional transition metal dichalcogenides from monolayer, multilayer to bulk material.* Chemical Society Reviews 44, 2757–2785 (2015).

[Zhu15] X. Zhu, N. R. Monahan, Z. Gong, H. Zhu, K. W. Williams, & C. A. Nelson. *Charge Transfer Excitons at van der Waals Interfaces.* Journal of the American Chemical Society 137, 8313–8320 (2015).

Acknowledgements

I would like to thank Dr. Ralph Ernstorfer for the possibility to write my master's thesis in his group, and for his help and his patience in answering my many questions.

I thank Thomas Vasileiadis for showing me how to measure with the time-resolved diffraction setup and for a lot of help during the measurements and with the interpretation of the data.

Furthermore, I would like to thank Dr. Lutz Waldecker for sharing his knowledge about electron diffraction with me and for many helpful suggestions regarding the sample preparation.

I would also like to thank Prof. Dr. Martin Wolf, the director of the physical chemistry department of the FHI.

Thanks to Dr. Ilya Razdolski and to Dr. Alexey Melnikov for performing the time-resolved optical experiments on the WSe_2 sample, for sharing their knowledge about this type of experiments and for helping me with the interpretation of the data.

I would like to thank Dr. Georg Simon and Dr. Markus Heyde for measuring the thickness of my WSe_2 and WS_2 samples with their atomic force microscope.

Thanks to Pascal Thuge for helping me with the sample preparation.

Thanks to Melanie Müller, Faruk Krecinic and Jannik Malter for helpful discussions, and thanks to all members of the structural and electronic surface dynamics group for the nice working atmosphere.

Last, but not least, thanks to my family for their support during my studies.

Eidesstattliche Erklärung

Ich versichere hiermit an Eides statt, dass diese Arbeit von niemand anderem als meiner Person verfasst worden ist. Alle verwendeten Hilfsmittel wie Berichte, Bücher, Internetseiten oder ähnliches sind im Literaturverzeichnis angegeben, Zitate aus fremden Arbeiten sind als solche kenntlich gemacht. Die Arbeit wurde bisher in gleicher oder ähnlicher Form keiner anderen Prüfungskommission vorgelegt und auch nicht veröffentlicht.

Daniela Zahn